Nucleotide depletion promotes cell fate transitions by inducing DNA replication stress

Peggy P. Hsu[1,2,3,5,*,+], Brian T. Do[1,4,5,*], Sidney Y. Vermeulen[1,6], Zhishan Wang[1,5], Taghreed Hirz[3], Najihah Aziz[3], Joseph M. Replogle[7,8], Keene L. Abbott[1,5], Samuel Block[1,5], Alicia M. Darnell[1,5], Raphael Ferreira[1,9], Jelena Milosevic[3], Daniel R. Schmidt[1,5,10], Christopher Chidley[11], Xiaofeng A. Su[1,5], Isaac S. Harris[12], Jonathan S. Weissman[5,7,13], Sihem Cheloufi[14,15], David B. Sykes[3,16,17], Matthew G. Vander Heiden[1,2,5,++]

[1]Koch Institute for Integrative Cancer Research, Massachusetts Institute of Technology, Cambridge, MA 02139, USA

[2]Dana-Farber Cancer Institute, Boston, MA 02115, USA

[3]Massachusetts General Hospital Cancer Center, Boston, MA 02113, USA

[4]Harvard-MIT Health Sciences and Technology, Cambridge, MA 02139, USA

[5]Department of Biology, Massachusetts Institute of Technology, Cambridge, MA 02139, USA

[6]Department of Electrical Engineering and Computer Science, Massachusetts Institute of Technology, Cambridge, MA 02139, USA

[7]Whitehead Institute for Biomedical Research, Cambridge, MA 02139, USA

[8]Medical Scientist Training Program, University of California, San Francisco, CA 94158, USA

[9]Department of Genetics, Harvard Medical School, Boston, Massachusetts, USA

[10]Department of Radiation Oncology, Beth Israel Deaconess Medical Center, Boston, MA 02215, USA

[11]Laboratory of Systems Pharmacology, Harvard Medical School, Boston, MA 02115, USA

[12]Wilmot Cancer Institute, University of Rochester Medical Center, Rochester, NY 14642, USA

[13]Howard Hughes Medical Institute, Cambridge, MA 02139, USA

[14]Department of Biochemistry, University of California, Riverside, CA 92521, USA

[15]Stem Cell Center, University of California, Riverside, CA 92521, USA

[16]Center for Regenerative Medicine, Massachusetts General Hospital, Boston, MA 02113, USA

[17]Harvard Stem Cell Institute, Cambridge, MA 02139, USA

*These authors contributed equally to this work.

+Present address: Rogel Cancer Center, University of Michigan, Ann Arbor, MI 48109, USA and Department of Gastroenterology, Internal Medicine, University of Michigan, Ann Arbor, MI 48109

++Correspondence: mvh@mit.edu

ABSTRACT

Control of cellular identity involves coordination of developmental programs with environmental factors such as nutrient availability, suggesting that modulating aspects of metabolism could enable therapeutically relevant changes in cell fate. We show that nucleotide depletion facilitates gene expression changes towards a new cell fate by perturbing DNA replication in models of acute myeloid leukemia, a cancer characterized by a differentiation blockade. This transition starts in S phase and is independent of replication stress signaling and DNA damage signaling pathways. Moreover, it occurs despite sustained oncogene-driven expression of the progenitor program and is accompanied by limited changes in chromatin accessibility. Altering lineage-determining transcription factor expression redirects cell fate progression towards an alternate fate upon replication stress, suggesting that perturbing DNA replication allows cells to mobilize primed maturation programs. Our work, along with other findings in diverse systems, suggests a conserved mechanism by which metabolic changes can orchestrate cell fate transitions.

INTRODUCTION

Mammalian cells must tightly regulate cell identity to ensure proper development and maintenance of tissue homeostasis (Intlekofer and Finley, 2019; Shapira and Christofk, 2020). Various processes integrate a diverse set of external cues and markers of internal state with cell type-specific developmental programs, ultimately guiding a decision to self-renew or to differentiate towards a particular cellular identity. Dysregulation of cellular identity lies at the root of a wide range of processes including cancer progression and the development of treatment resistance, underscoring the therapeutic potential of novel strategies to deterministically drive changes in cell fate (Le Magnen et al., 2018; Quintanal-Villalonga et al., 2020; Roy and Hebrok, 2015).

It has been increasingly recognized that the set of external cues driving cell fate decisions includes not only ligands that activate developmental signaling pathways (Perrimon et al., 2012), but also the availability of environmental nutrients (Baksh and Finley, 2021; Lin et al., 2018). Metabolic profiling and systematic identification of metabolic vulnerabilities in different cell types or stages of differentiation across various systems have demonstrated that nutrient availability can not only gate, but also influence, lineage decisions (Gonzalez-Menendez et al., 2021; Oburoglu et al., 2014; Sharpley et al., 2021; Solmonson et al., 2022). While the mechanistic connections between metabolism and cell fate change remain unclear, a few metabolic perturbations have been found to directly alter the levels of metabolites that act as substrates or cofactors for enzymes that control epigenetic marks on chromatin (Baksh and Finley, 2021; Meier, 2013). Intriguingly, the same perturbation can often promote or suppress lineage progression depending on the cell type and environmental context (Carey et al., 2015;

2

TeSlaa et al., 2016). Nevertheless, a comprehensive understanding of how changes in metabolism can promote specific cell fate transitions in different cell types is lacking.

One disease where the ability to direct cell fate has therapeutic potential is acute myeloid leukemia (AML), a cancer characterized by uncontrolled proliferation of undifferentiated myeloid precursors (Döhner et al., 2017). A differentiation block leading to AML can be triggered by a wide variety of genetic events that either reduce the activity of lineage-determining transcription factors (TFs) or constitutively activate progenitor-specific regulatory networks (Papaemmanuil et al., 2016). When paired with mutations that increase proliferative capacity, hematopoietic stem and progenitor cells are ultimately arrested in an immature state of self-renewal. Targeted therapies that relieve the differentiation blockade have been transformative in the treatment of certain genetically defined subsets of AML, such as acute promyelocytic or IDH-mutant leukemias, yet broad strategies to overcome differentiation arrest are still lacking for most other AML subsets as well as solid tumors (de Thé, 2018; Wang et al., 2021).

Inhibitors of the pyrimidine biosynthetic enzyme dihydroorotate dehydrogenase (DHODH) have been identified as a novel class of differentiation agents in non-promyelocytic and non-IDH mutated AML (Sykes et al., 2016). As a result, DHODH inhibitors are currently being evaluated for the treatment of AML and other cancers (Christian et al., 2019; Zee et al., 2021). These studies raise the question of how pyrimidine depletion can induce a cell fate change and, more broadly, whether other therapeutic strategies that target metabolism might be similarly effective.

Here, we systematically searched for metabolic perturbations that lead to differentiation in distinct models of AML with different oncogenic alterations. We find that depletion of either purines or pyrimidines initiates lineage-specific maturation programs by lowering dNTP levels and perturbing DNA replication. These transitions begin during S phase but do not depend on signaling through the ATR/Chk1 replication stress response or the DNA-damage response, suggesting a direct role for altered DNA replication dynamics in enabling a change in gene expression. Replication stress-induced differentiation transpires despite continued expression of the progenitor program, and moreover is transcription factor (TF) agnostic, as altering the availability of specific lineage-defining TFs simply redirects the differentiation response to an alternative lineage. Altogether, these data suggest that metabolic stresses impinging on DNA replication are sufficient to allow cells to circumvent obstacles to cell fate change.

3

RESULTS

Perturbing nucleotide metabolism can promote leukemia differentiation

To begin to study how changes in metabolism can impact cell identity, we took advantage of a model of acute myeloid leukemia where differentiation of murine granulocyte-macrophage progenitor (GMP) cells is blocked by expression of an estrogen receptor-homeobox transcription factor Hoxa9 (ER-Hoxa9) fusion protein in the presence of estradiol (E2) (Figure 1A) (Sykes et al., 2016). Hoxa9, a progenitor transcription factor that is normally downregulated during myeloid differentiation, is overexpressed in over half of AMLs driven by a variety of genetic alterations and directly promotes leukemogenesis (Collins and Hess, 2016). Upon E2 withdrawal or ER antagonism, ER-Hoxa9 activity is curtailed and the ER-Hoxa9 GMP cells terminally differentiate into neutrophils (Christian et al., 2019; Sykes et al., 2016). In this model, green fluorescent protein (GFP) is also expressed from the lysozyme M (*Lyz*) locus upon differentiation (Faust et al., 2000). This model is amenable for screening for compounds that drive differentiation, as a single-dose chemical screen involving a largely unannotated small molecule library previously found that inhibitors of dihydroorotate dehydrogenase (DHODH), an enzyme required for the pyrimidine synthesis, could promote differentiation (Sykes et al., 2016).

To identify other metabolic perturbations that can promote differentiation, we used the ER-Hoxa9 GMPs to perform a targeted flow cytometry screen with a curated library of 240 small molecule inhibitors of various classes of metabolic enzymes, where cells were treated over a 10-point dose range of each inhibitor (Figure 1B-C, Table S1) (Harris et al., 2019). Differentiation was assessed with GFP fluorescence, indicating induction of the neutrophil gene lysozyme, and expression of the myeloid surface marker CD11b. Among compounds that were found to promote GFP and CD11b expression, the majority targeted nucleotide biosynthesis enzymes (Figure 1B-D), including the DHODH inhibitors brequinar (BRQ) and leflunomide as well as additional hits that targeted both pyrimidine synthesis (such as cyclopentenyl cytosine, 5-fluorouracil, and pyrazofurin) and purine synthesis (such as mycophenolic acid, mercaptopurine, and 6-thioguanine). Differentiation was also induced by antifolates (pyrimethamine, methotrexate, and raltitrexed), which inhibit folate-requiring enzymes in purine and/or thymidine synthesis, and nucleoside analogues (cytarabine, cladribine, and 5-fluorouracil) that can both incorporate into nucleic acid polymers and inhibit various nucleotide biosynthetic enzymes.

Among differentiation-inducing compounds that were not primarily annotated as nucleotide metabolism inhibitors (Figure 1D), several had proven or likely effects on nucleotides, including acivicin, a glutamine analog that could inhibit nucleotide biosynthesis (Kensler et al., 1982), and plumbagin, which has been shown to inhibit pyrimidine biosynthesis (Guan et al., 2021). In contrast to nucleotide synthesis inhibitors, most other metabolic inhibitors tested had no effect on differentiation marker expression

(Figure 1D). Specifically, inhibitors of the electron transport chain (rotenone and oligomycin), NAD+ biosynthesis (FK866 and GPP78), ER stress (CCF642, thapsigargin, and tunicamycin), and lipid synthesis (GSK2194069) did not induce differentiation markers (Figure S1A).

To understand the metabolic effects of these nucleotide-depleting agents, we performed liquid chromatography-mass spectrometry (LC-MS) on ER-Hoxa9 cells treated with various inhibitors of *de novo* purine or pyrimidine nucleotide biosynthesis. Levels of specific ribonucleotide triphosphates (NTPs) and deoxyribonucleotide triphosphates (dNTPs) were depleted following treatment (Figure 1E, Figure S1B-C, Table S2). Supplementation with the appropriate nucleobase or nucleoside rescued both NTP and dNTP levels and prevented differentiation caused by drug treatment (Figure 1E-F, Figure S1B-C).

To identify metabolic pathways that might modulate the ability of nucleotide synthesis inhibition to induce differentiation, we repeated the metabolic inhibitor screen in ER-Hoxa9 GMP cells in the presence of a dose of BRQ (500 nM) that only induces partial differentiation and has minimal effect on viability. Most of the drugs that amplified the effects of BRQ were pyrimidine inhibitors (Table S1, Figure S1D). On the other hand, suppressors of BRQ-induced differentiation included a variety of purine synthesis inhibitors, inducers of endoplasmic reticulum stress, mitochondrial inhibitors, and drugs involved in redox metabolism (Figure S1E). Validation of some of these compounds revealed that many nonspecifically inhibited differentiation caused by both BRQ and fulvestrant, an estrogen receptor antagonist that represses ER-Hoxa9 activity (Figure S1F), whereas the purine synthesis inhibitors lometrexol (a GART inhibitor) and azaserine (a glutamine analog/GPAT inhibitor) specifically suppressed BRQ-induced differentiation (Figure S1G). Thus, the finding that differentiation caused by BRQ, a pyrimidine synthesis inhibitor, synergizes with other pyrimidine inhibitors but is suppressed by purine inhibitors suggests that proper balance among different nucleotide species may be important for maintaining the progenitor state.

To directly test whether nucleotide imbalance could drive differentiation, we supplied cells with exogenous nucleotides (Diehl et al., 2021). Interestingly, addition of high levels of extracellular adenine (A) or thymidine (T) alone led to differentiation, while excess guanine (G), cytidine (C) or uridine (U) did not induce differentiation (Figure 1G). LC-MS in ER-Hoxa9 cells revealed that excess A, G, or T led to significant depletion of at least one dNTP species without necessarily depleting any NTP species, and the effect of G was less severe than that of A or T (Figure S1H, Table S2). Indeed, NTP excess or imbalance can be sufficient to suppress synthesis of specific dNTPs through feedback inhibition on ribonucleotide reductase (Brignole et al., 2018; Diehl et al., 2021). Together, these data suggest that various nucleotide perturbations that alter dNTP levels can also promote differentiation in these cells.

5

Finally, we tested whether perturbing nucleotide metabolism could induce differentiation in other AML models. THP-1 and U937 human AML cell lines can differentiate down a monocytic lineage (Daigneault et al., 2010). Both purine and pyrimidine synthesis inhibitors, and addition of select exogenous nucleotide species, induced macrophage surface markers, including CD11b and CD16, in these cells (Figure 1H, S1I-J). In K562 human erythroleukemia cells, which can differentiate down an erythroid lineage (Uchida et al., 2018), nucleotide depletion with BRQ treatment increased surface expression of the erythroid marker CD235a (glycophorin A) (Figure 1I). Thus, perturbing nucleotide metabolism is a route to differentiation in multiple leukemic models.

Replication stress links nucleotide depletion to differentiation

Given the convergence of data correlating dNTP depletion and NTP balance with nucleotide inhibitor-induced differentiation, we hypothesized that effects on DNA replication might be contributing to this phenotype. To test this, we directly inhibited ribonucleotide reductase (RNR), the enzyme necessary to synthesize dNTPs for DNA replication, using hydroxyurea (HU), gemcitabine, clofarabine, or 3-AP and found that these RNR inhibitors promoted differentiation of ER-Hoxa9, THP-1, U937, and K562 cells (Figure 2A, S2A-C). We confirmed that HU treatment affected dNTP levels without affecting NTP levels (Figure 2B, S2D, Table S2). To assess whether defects in DNA replication might be involved in promoting differentiation downstream of altered dNTP levels, we directly inhibited DNA polymerase using aphidicolin (APH) and found that this also led to differentiation (Griffin et al., 1982) without reducing dNTP levels (Figure 2A-B, S2E). In addition to inducing maturation-related changes in surface marker expression, BRQ, HU, and APH led to morphological changes consistent with differentiation, such as granule formation, an increased cytoplasmic to nuclear ratio, and ringed or multilobed nuclei (Figure S2F).

Decreased dNTP levels or inhibition of DNA polymerase lead to slower replication fork progression, reduced replication fidelity, and DNA strand breaks in a phenomenon broadly termed replication stress (Zeman and Cimprich, 2014). Accordingly, multiple markers of replication stress were evident as a result of BRQ, HU, and APH treatment, including a decrease in the rate of 5-ethynyl-2-deoxyuridine (EdU) incorporation in S phase cells (Figure 2C-D, S2G-H), phosphorylation of histone H2AX (γH2AX) and the ATR target Chk1 (Figure S2I-J). BRQ and HU also led to increased numbers of γH2AX and RPA nuclear foci (Figure 2E-F) (Saxena and Zou, 2022). In ER-Hoxa9 cells, phosphorylated Chk1 and γH2AX also occurred upon addition of excess A or T, which promoted differentiation, but not upon addition of C, G, and U, which did not induce differentiation (Figure S2K-L). Taken together, these data suggest that DNA replication stress links nucleotide depletion with differentiation in these cells.

6

Brequinar treatment *in vivo* is known to induce differentiation markers in several leukemia models (Christian et al., 2019; Sykes et al., 2016). To explore whether replication stress can also induce differentiation in vivo, we injected THP-1 cells subcutaneously into nude mice and treated them intraperitoneally with vehicle or 50 mg/kg BRQ once measurable tumors formed (Figure 2G). After three days, we observed a significant decrease in tumor growth in response to BRQ (Figure 2H). Leukemia cells from these tumors exhibited increased CD11b and CD14 surface marker expression (Figure 2I). Concomitantly, these cells also had higher levels of phosphorylated Chk1 and γH2AX as measured by flow cytometry (Figure 2J-K). Thus, BRQ treatment also induces DNA replication stress alongside differentiation of leukemia *in vivo*.

Genetic perturbation of DNA replication can promote differentiation

To identify genetic modulators of differentiation in the setting of nucleotide depletion, we combined BRQ treatment with a flow cytometry-based genome-wide CRISPR interference (CRISPRi) screen in human THP-1 dCas9-KRAB cells. Cells were treated for 48 hours with 500 nM BRQ, a concentration at which approximately 50% of cells induce CD11b expression (Figure 3A). By using flow cytometry to sort the top and bottom 25% of CD11b-expressing cells and comparing guide enrichment, we identified genes whose knockdown prevented or further sensitized cells to BRQ-mediated induction of CD11b expression (Figure 3B, S3A, Table S3). Genes whose knockdown weakened CD11b induction by BRQ included general transcription factors and transcriptional/chromatin machinery (Figure S3A), which may reflect nonspecific requirements for transcriptional initiation and a change in marker expression.

Genes that promoted CD11b expression in response to BRQ included those involved in ribosome biogenesis, mRNA splicing, chromatin modifiers, and DNA replication and S phase (Figure 3B-C, S3B). In particular, increased CD11b expression was sensitized by knockdown of DNA-replication related genes, including proteins required for origin recognition (MCM2, MCM3, ORC5), the lagging-strand DNA polymerase δ holoenzyme (POLD1 and POLD3), and helicases and accessory components (RFC4, GINS3) (Figure S3B). Reduced origin firing itself can cause replication stress or sensitize cells to replication stress by impairing the ability of cells to access backup origins (Alvarez et al., 2015; Ibarra et al., 2008). We also found that knockdown of various genes involved in processes that can affect nucleotide levels sensitized cells to BRQ-induced differentiation upon knockdown. These included genes involved in multiple branches of nucleotide biosynthesis, including pyrimidines (CAD, UMPS, TYMS, CTPS1), purines (ATIC, GART, PAICS), and dNTPs (RRM1). Additionally, we identified hits within oxidative phosphorylation (complex I components), aspartate synthesis (GOT2), and heme/iron metabolism (FECH, HSCB, ABCB7, and TFRC), all pathways that can be important for nucleotide biosynthesis (Birsoy et al., 2015; Schwartz et al., 2021; Sullivan et al., 2015) (Figure S3B). When we reanalyzed data from a previously reported screen in untreated THP-1 cells (Wang et al., 2021),

depletion of S-phase and nucleotide biosynthesis genes was also found to drive CD11b expression, consistent with our results and suggesting that direct perturbation of DNA replication alone can induce myeloid differentiation (Figure S3C, Table S3).

To validate select hits from the CRISPRi screen and confirm that they both perturb DNA replication and promote differentiation, we performed single gene knockdowns of the replication-related genes POLD3, MCM2, and RFC4, the iron-sulfur cluster transporter ABCB7, and the transaminase GOT2 using single-gene CRISPRi in THP-1 cells (Figure S3D-E). Knockdown of these genes all decreased EdU incorporation in S phase cells, suggestive of DNA replication stress (Figure 3D). The percentage of CD11b+ cells was increased compared to cells expressing non-targeting sgRNAs (sgNTC), and BRQ and HU treatment caused further CD11b induction (Figure S3F-G). Gene set enrichment analysis (GSEA) revealed significant upregulation of genes that are induced by the differentiation agent phorbol 12-myristate 13-acetate (PMA) (Figure 3E), including multiple markers of monocyte-to-macrophage differentiation (*MAFB*, *SLC15A3*, *CD86*, *CD163*, and *PLIN2*), as well as downregulation of monocytic genes (*CTSG* and *MS4A3*) (Figure S3H).

To test whether disrupting DNA replication also induces cell fate progression in K562 cells, we re-analyzed a Perturb-seq experiment in these cells where single-cell RNA-seq was performed for CRISPRi knockdown of most human genes (Replogle et al., 2022) (Figure 3F, S3I, Table S3). While K562 cells are derived from an erythroleukemia line, have characteristics of erythroid precursors, and tend to differentiate down an erythroid lineage, they can also acquire myeloid characteristics in response to specific stimuli (Sutherland et al., 1986), affording us the additional opportunity to test whether disrupting DNA replication is selective for maturation along a particular lineage in these cells. Each knockdown was scored by degree of induction of an erythroid signature (marker genes included *HBZ* and *SLC25A37*) or a myeloid signature (marker genes included *SPI1* and *CSF3R)*. Knockdown of genes involved in DNA replication and nucleotide synthesis, such as POLD3, GINS4, and GART, led to high erythroid, but not myeloid, scores, as did knockdown of the oncogenic driver BCR-ABL using guides targeting the *BCR* promoter (Figure 3G, S3J-K). This enrichment for genes related to nucleotide synthesis and DNA replication within the top-scoring erythroid transcriptomes stood in stark contrast to genes whose knockdown led to a high myeloid score, most of which were transcription factors (such as the erythroid TF GATA-1) or epigenetic machinery (such as KDM1A and the Integrator components INTS2 and INTS5) (Figure 3G-H). Notably, many hits with a high erythroid score were also hits for macrophage differentiation in our THP-1 CRISPRi screen (Figure 3I, Table S3). Together, these results indicate that genetically perturbing DNA replication induces maturation toward an already primed fate (e.g. macrophage in THP-1 or erythroid in K562), in contrast to perturbations in other pathways that can expand cell fate towards other lineages.

8

Nucleotide depletion induces differentiation during S phase of the cell cycle

Given the effect of perturbing DNA replication on differentiation, we wondered whether the timing of initiation of the differentiation program could provide insight. Using ER-Hoxa9 cells co-expressing the differentiation reporter lysozyme-GFP and the FUCCI geminin-mCherry reporter, which marks cells in S/G2/M phase (Sakaue-Sawano et al., 2008), we found that mCherry-positive cells were the first to exhibit GFP expression following BRQ or HU treatment (Figure 4A, S4A). At later timepoints, a notable percentage of GFP+ cells was evident in the mCherry-negative G0/G1 fraction, likely as a result of cell division. On the contrary, ER-Hoxa9 inactivation with fulvestrant allowed cells to differentiate preferentially from G1 without necessarily having transited S phase following drug addition (Figure 4A, S4A). We further localized the onset of BRQ-induced differentiation to S phase, as 90% of CD11b+ cells also displayed EdU incorporation at the 16-hour timepoint (Figure 4B). As an orthogonal method of linking cell-cycle stage to differentiation status, we performed single-cell RNA sequencing at various timepoints. Consistent with our flow cytometry results, we found that the majority of cells 24 hours after BRQ treatment were localized in S or G2 phase while also scoring highly for a "granulocyte signature" consisting of genes such as *Spi1*, *Fcgr3*, and *Gsn* (Figure 4C-D, S4B). This was in contrast to ER-Hoxa9 inactivation via E2 withdrawal, where cells with a granulocytic gene expression signature were not localized to any particular cell cycle phase.

We next asked whether S phase entry is required for nucleotide depletion-induced differentiation. To test this, we prevented entry of ER-Hoxa9 cells into S phase by withdrawing the growth factor SCF (Figure 4E). Indeed, limiting S phase entry completely blocked differentiation upon BRQ treatment in contrast to ER-Hoxa9 inactivation with fulvestrant (Figure 4F). Together, these results demonstrate that nucleotide depletion-induced differentiation initiates only during S phase.

Differentiation is induced by perturbed DNA replication independently of replication stress response signaling or DNA damage

Initiation of the differentiation program during S phase prompted us to investigate the contribution of processes that occur during this phase of the cell cycle. When DNA replication is interrupted, exposed single-stranded DNA accumulates and is rapidly bound by RPA, leading to ATR activation and subsequent Chk1 phosphorylation to inhibit cell cycle progression and suppress late origin firing (Zeman and Cimprich, 2014). Stressed replication forks can collapse and yield DNA breaks, which activate repair machinery and signaling pathways including ATM, which phosphorylates both Chk1 and Chk2. Given the reported links between ATR/ATM signaling and induction of certain lineage-determining factors (Atashpaz et al., 2020; Sherman et al., 2010), we hypothesized that these pathways might play a role in initiating differentiation. However, knockdown of the signaling components ATR, ATM, CHEK1, and CHEK2 in the CRISPRi screen did not rescue BRQ-mediated

differentiation in THP-1 cells (Figure 4G). To extend these findings, we determined the lowest dose of ATR and/or ATM inhibitors to the lowest dose that reduced Chk1 S345 phosphorylation to baseline in both ER-Hoxa9 and THP-1 cells (Figure S4C-D). We found that these inhibitors did not suppress CD11b expression differentiation caused by BRQ or APH, and in some cases they potentiated differentiation, indicating that the replication stress signaling response is not required for differentiation induced by replication stress (Figure 4H, S4E). Notably, while there was no effect in ER-Hoxa9 cells, ATR inhibition in vehicle-treated THP-1 cells led to low levels of differentiation, demonstrating that exacerbation of endogenous replication stress by ATR inhibition is sufficient to induce differentiation in some cells (Figure S4E) (Santos et al., 2014; Toledo et al., 2013). Pharmacologic suppression of Chk1 activity also did not inhibit differentiation (Figure 4H).

The cyclin-dependent kinase inhibitor p21 (*Cdkn1a*) is an important target of Chk1 signaling that suppresses G1/S progression and whose transcript levels are rapidly upregulated upon nucleotide depletion (Figure S4G-H). p21 has been implicated in inducing differentiation in myeloid cells, potentially by lengthening G1 or enabling accumulation of the transcription factor PU.1 (Kueh et al., 2013; Santos et al., 2014). However, CRISPRi-mediated knockdown of p21 also did not suppress differentiation caused by BRQ or APH in either ER-Hoxa9 or THP-1 cells, consistent with our earlier results demonstrating that differentiation initiates during S phase (Figure 4I, S4I-K). Furthermore, G1 arrest caused by withdrawal of SCF did not cause differentiation in ER-Hoxa9 cells (Figure 4F).

DNA damage has been linked to cell fate changes in several systems (Grow et al., 2021; Inomata et al., 2009; Kato et al., 2021; Molinuevo et al., 2020; Santos et al., 2014; Wang et al., 2012). To directly test whether DNA damage can cause differentiation in these cells, we used various DNA damaging agents. The interstrand crosslinker cisplatin, the DNA topoisomerase inhibitor etoposide, and the DNA intercalator daunorubicin all induced CD11b expression, as did gamma-irradiation (Figure S4L-M). Notably, exposure to DNA damaging agents or the double-stranded break inducer neocarzinostatin (NCS) also caused replication stress, as evidenced by decreased EdU incorporation during S phase as well as an increased number of RPA foci (Figure S4N-O). To test whether DNA damage could drive differentiation independently of replication stress, we arrested cells in G1 via SCF withdrawal then added NCS, which can induce DNA double-stranded breaks during all phases of the cell cycle (Figure 4J, S4P) (Liu et al., 2020). As expected, markers of DNA damage, including increased number of γH2AX foci and nuclear intensity, were elevated in both G1-arrested and asynchronously cycling cells after NCS treatment (Figure 4K, S4Q-S). However, differentiation did not occur when G1-arrested cells were challenged with NCS (Figure 4L). Cisplatin, which creates DNA adducts that can be sensed and repaired at all phases of the cell cycle, also did not cause differentiation of G1-arrested cells even though 20% had at least five γH2AX foci (Figure 4K-L, S4P-S). Together, these results argue that

replication stress itself is the driver of differentiation, rather than downstream consequences such as activation of checkpoint signaling, G1 lengthening, or DNA damage.

Replication stress induces a maturation program without fully inactivating progenitor programs

To understand how the cell fate change induced by replication stress compares to that caused by suppression of the oncogene-enforced differentiation block, we first compared bulk RNA-seq data over time from ER-Hoxa9 cells following either BRQ treatment or Hoxa9 inactivation via E2 withdrawal. Both treatments exhibited expression changes in thousands of genes, with more extensive transcriptome remodeling at later timepoints following E2 withdrawal (Figure 5A, S5A, Table S4). Within 24-48 hours, cells exposed to both perturbations progressed to a more differentiated state characterized by genes involved in neutrophil activation and regulation of inflammatory response, such as primary granule genes (*Mpo*, *Elane*, and *Prss57*) (Figure 5B, S5B). However, unlike cells where Hoxa9 activity was lost, BRQ-treated cells did not downregulate GMP/progenitor transcription factors and markers (*Flt3, Meis1, Cd34*) and alternate-lineage (B and T cell) genes (*Ebf1*, *Thy1*, *Rag1*) (Figure 5B, S5C). In BRQ-treated cells, we also observed consistent upregulation of normally transiently expressed genes such as *Mpo* and *Prtn3* as well as weaker (or no change in) expression of late-differentiation markers (*Lcn2*, *Camp*, *Lyn*, *Fpr1*) even by 96 hours (Figure 5B) (Lehman and Segal, 2020; Muench et al., 2020). Comparison with single-cell transcriptomes of normal murine neutrophil precursors demonstrated that unlike E2 withdrawal, which drove steady differentiation, BRQ treatment led to transcriptomes that appeared to stall at an intermediate stage (Xie et al., 2020) (Figure 5C). Using cleavage under targets and release using nuclease (CUT&RUN), we mapped ER-Hoxa9 binding sites on chromatin and found that they were retained during BRQ treatment, unlike in E2 withdrawal where almost all peaks disappeared (Figure S5D-E). Genes that were downregulated by E2 withdrawal but not BRQ, including the progenitor factors *Flt3*, *Meis1*, and *Ebf1*, were two-fold enriched for ER-Hoxa9 binding at baseline (Figure S5F-G). Thus, replication stress initiates a granulocytic maturation program despite continued activity of the Hoxa9-driven oncogenic program.

We next asked whether similar features governed the effect of replication stress on THP-1 cells after BRQ and HU treatment when compared to the differentiation agent PMA, which is known to downregulate the oncogenic driver MLL-AF9 (Pession et al., 2003) (Figure S5H, Table S4). All three perturbations increased mRNA levels of genes associated with monocyte-to-macrophage differentiation (*MAFB*, *CD163*, *CD36*) and downregulated the expression of some cell-cycle and monocytic progenitor genes (*NPM1*, *IRF8*, and *FLT3*) (Figure 5D). However, BRQ and HU treatment further activated granulocytic genes (*ITGAM*, *LYZ*, *LYN*) and did not downregulate important leukemia progenitor genes (*MYB*, *KLF4*, *ZFP36L2*), two categories of genes that were suppressed by PMA treatment (Phanstiel et al., 2017, 2009; Wang et al., 2021; Zhao et al., 2014). CRISPRi of DNA replication machinery

components similarly induced macrophage and granulocyte-related genes without extensive suppression of the progenitor state (Figure S3H).

Finally, we compared gene expression in K562 cells following BRQ treatment compared to CRISPRi knockdown of BCR-ABL using guides targeting the *BCR* promoter, which induces an erythroid transcriptional signature as well as the CD235a erythroid marker (Figure 3I, S5I-J). BRQ treatment did not suppress BCR-ABL expression (Figure S5J), yet both perturbations strongly induced genes involved in heme biosynthesis and erythroid differentiation (*SLC25A37*, *HBA1*, *RHCE*) and downregulated myeloid genes (*FCGR2A*, *LGALS1*, *LITAF*) and transcription factors (*MYB*, *EGR1*, *ETV4*) that mark a more immature state (Figure 5E, S5K, Table S4). BRQ treatment only weakly induced other erythroid genes (*CPOX, GYPA, SPTB*) and led to retained or elevated expression of progenitor TFs (*GATA2*, *SPI1*, *MECOM*), myeloid genes (*AIF1*, *LYZ*, *CD24*), and mitochondrial machinery (*TOMM*/*TIMM* protein import genes and *MRPL*/*MRPS* mitochondrial ribosome genes) (Caielli et al., 2021) (Figure 5E, S5K). Gene set enrichment analysis (GSEA) confirmed that genes normally downregulated during maturation of primary human erythroblasts were less robustly repressed by BRQ treatment than by sgBCR (Figure S5L) (Ludwig et al., 2019). Thus, replication stress weakens the BCR-ABL differentiation blockade, promoting erythroid maturation without fully downregulating the progenitor state.

Transcriptional rewiring during replication stress is accompanied by limited changes in chromatin accessibility

To examine whether replication stress influences chromatin accessibility to initiate a maturation program, we performed ATAC-seq across the early stages of differentiation induced by both BRQ and E2 withdrawal-mediated Hoxa9 repression in ER-Hoxa9 cells. Treatment with BRQ altered the accessibility landscape much less than differentiation triggered by E2 withdrawal (Figure 5F). Chromatin accessibility changes were also smaller in magnitude, skewed towards gains in accessibility following BRQ treatment (71% compared to 54% in E2 withdrawal), and initiated later following BRQ treatment (between 24 and 36h) than following E2 withdrawal (between 12 and 24h) (Figure 5G, S6A). In both treatments, differentially accessible peaks were enriched within introns and intergenic regions, consistent with distal regulatory regions such as enhancers playing important roles in driving cell fate progression (Figure S6B) (Blanco et al. 2021). We also observed similar patterns in THP-1 cells treated with BRQ compared to PMA over 48 hours, with subtler chromatin changes that were also predisposed towards gains in accessibility and localized mainly at distal regulatory loci (Figure 5H, S6C-D).

We next examined the functional consequences of such accessibility changes by calculating transcription factor (TF) motif accessibilities at open chromatin regions (Schep et al., 2017). Motifs for

the important myeloid TF PU.1 (Sfpi1/Spi1) began to gain accessibility within 12 hours of both BRQ treatment and E2 withdrawal (Figure 5G, Figure S6E). However, motif accessibility for the neutrophil-specifying Cebp family members, particularly CEBPa and CEBPe, was only weakly induced by BRQ. Moreover, consistent with retained progenitor TF expression, BRQ treatment in ER-Hoxa9 cells did not reduce accessibility at motifs for Hoxa9, its target Meis1, or progenitor/alternative lineage TFs within the Ebf, Runx, and Gata families. In THP-1 cells, AP-1 and bZIP family TFs, which play key roles in differentiation (Phanstiel et al., 2017, 2009), gained accessibility after both BRQ and PMA treatment, but several Hox family motifs were gained only in response to PMA (Figure 5I, S6F). Notably, BRQ treatment was unable to decrease accessibility at monocyte progenitor-specifying TFs such as CEBPD and IRF family members. Thus, replication stress opens chromatin targets for a subset of relevant lineage-specifying TFs while maintaining, and sometimes mildly increasing, the motif accessibility of many progenitor TFs.

Many maturation-related genes, including *Slpi* and *Csf2rb*, were highly upregulated by BRQ treatment in ER-Hoxa9 cells despite exhibiting relatively unchanged chromatin accessibility at the same timepoint (Figure 5J). To assess the extent of this discordance genome-wide, each putative regulatory locus (an ATAC-seq peak with H3K4me1 signal) was assigned to the nearest transcriptional start site within 100 kilobases (Kiani et al. 2022; Sanford et al. 2020). Among genes that were upregulated to similar degrees after BRQ treatment or E2 withdrawal, smaller increases in accessibility at associated regulatory loci occurred as a result of BRQ treatment (Figure 5K, S6G). In THP-1 cells, shared upregulated genes (such as *AIM2* and *MERTK*) were also less inclined to gain accessibility during BRQ compared to PMA treatment (Figure S6H-I). Reduced concordance between transcriptional changes and local accessibility was also seen genome-wide during replication stress (Figure S6J-K). Together, these observations indicate that replication stress can induce expression of maturation-related genes without enacting proportional changes in chromatin accessibility.

Cell fate progression driven by replication stress is influenced by the preexisting transcription factor repertoire

Because lineage-specific TFs can also drive maturation programs by binding to already accessible chromatin, and progenitor cells are often primed towards specific lineages at the level of TF expression and chromatin landscape (Ma et al., 2020; Paul et al., 2015), we sought to explore how replication stress interfaces with the pre-existing TF repertoire to support cell fate progression. Our ATAC-seq analysis suggested a role for the myeloid regulator PU.1 (encoded by human *SPI1*/mouse *Sfpi1*) in replication stress-induced differentiation in ER-Hoxa9 cells (Figure 5G). PU.1 plays an essential role in normal myelomonocytic and lymphoid differentiation. Loss of function or decreased expression of PU.1 is associated with AML, and overexpression has been shown to restore differentiation (Durual et al.,

2007; Kueh et al., 2013; McKenzie et al., 2019). Although PU.1 was already highly expressed at baseline in these cells, its expression as well as that of its target genes increased even further after 12 hours of BRQ treatment (Figure S7A). To functionally test the necessity of PU.1 for differentiation, we knocked down PU.1 using CRISPRi (Figure S7B). Loss of PU.1 substantially impaired induction of CD11b expression by BRQ, HU, or APH (Figure 6A).

RNAseq revealed that PU.1 depletion also prevented upregulation of 300 genes by BRQ, including genes related to myeloid differentiation and known targets of PU.1, such as *Itgam*, *Tyrobp*, and *Ms4a3* (Figure 6B-C, S7C, Table S4). However, 262 new genes were activated by BRQ, many of which were part of the erythroid (*Gypa*, *Gata1*, *Car1*, *Epor*), mast cell/basophil (*Cma1*, *Prss34*), or T cell lineages (*Cd247* and *Trat1*) (Figure 6C, S7C). Thus, when PU.1 is absent, replication stress still promotes differentiation towards a new cell fate, but in a manner now characterized by induction of alternative hematopoietic lineage genes. Of note, expression of some of these genes was already increased to an extent following PU.1 knockdown, perhaps because other hematopoietic TFs such as GATA-1 become more active in the absence of PU.1 (Figure 6C).

We then tested this paradigm in erythroid-biased K562 cells, where our Perturb-seq data had indicated that knockdown of the erythroid TF GATA-1 reprograms these cells towards a myeloid fate (Figure 3G). We asked whether the maturation program induced by replication stress would reflect this new fate. GATA-1 knockdown cells did not exhibit increased surface expression of the erythroid differentiation marker CD235a following BRQ or HU treatment (Figure 6D, S7D, Table S4). After 72 hours of BRQ treatment, 563 genes, enriched for the erythroid lineage, were upregulated in control but not GATA-1 knockdown cells (Figure 6E, S7E). However, 89 genes were uniquely activated in GATA-1 knockdown cells, many of which were associated with the myeloid or lymphoid lineages (such as *NFKBID*, *FCRLA*, *CD4*, and *AIM2*) (Figure 6F, S7E). We note that the 65 genes upregulated in both settings were also enriched for erythroid genes, but their degree of induction was lessened in the GATA-1 knockdown background (Figure 6F). Taken together, these data suggest that rather than activating a specific TF, replication stress instead causes cells to initiate the lineage program delineated by the set of available TFs.

DISCUSSION

How metabolic cues influence cell fate transitions and whether these cues can be manipulated to treat pathologic cell states is an area of ongoing investigation (Baksh and Finley, 2020). We demonstrate in multiple leukemia models that perturbations that deplete nucleotides (pyrimidine, purine, or deoxynucleotide) and alter DNA replication dynamics can enable cell fate progression despite the

14

continued presence of oncogenic signaling. Disrupting the DNA replication machinery phenocopies these effects across leukemia models with oncogenic drivers of differentiation arrest.

While chemical inhibitors of nucleotide and DNA synthesis as well as DNA damage have previously been shown to induce expression of lineage-specific markers in leukemic cells (Ebert, 1976; Griffin et al., 1982; Gusella and Housman, 1976; Huang et al., 2004; Park et al., 2001; Santos et al., 2014), we now demonstrate at the transcriptomic and epigenetic level that replication stress activates TF-governed lineage programs and proceeds without full suppression of the progenitor program. Thus, rather than directly suppressing the cause of the differentiation arrest itself, replication stress appears to lower the barriers to activation of prespecified lineage programs in a manner that is dependent on the available transcription factors. Indeed, classic work in erythroid cells suggested roles for S phase-targeting agents in modulating maturation (Nathan, 1985; Rencricca et al., 1975), and recent studies in nontransformed systems (iPSC-derived cardiomyocytes, pancreatic endocrine differentiation, and *C. elegans* cell extrusion) have also suggested that replication stress and slowed replication fork speed can facilitate or accelerate cell fate progression (Dwivedi et al., 2021; Nakano et al., 2017; Sui et al., 2021). Notably, replication stress appears to shift mouse embryonic stem cells towards a less differentiated 2-cell-like cell (2CLC) fate (Atashpaz et al., 2020; Grow et al., 2021) and can facilitate reprogramming (Nakatani et al., 2022), emphasizing that perturbing DNA replication may not always lead cells to a more differentiated state, but rather may cause cells to have increased plasticity to mobilize available TFs and change cell fate.

Several studies have suggested an upstream role for the ATR/Chk1 replication stress signaling response in enabling fate transitions (Atashpaz et al., 2020; Santos et al., 2014; Tomic et al., 2022). However, our data demonstrate that genetic depletion or pharmacologic inhibition of ATR, Chk1, and p21 do not necessarily affect differentiation ability. Further work is needed to explain this differential requirement for ATR/Chk1 and DNA damage pathways for fate progression, and how these signaling cascades might be wired to lineage-specific transcriptional programs. Nevertheless, we favor a model whereby ATR and Chk1 are required for adaptation to and cell survival upon dNTP imbalance and replication stress (Diehl et al., 2022), and that instead, disruption of DNA replication itself may directly affect gene expression or the epigenetic landscape to enable cell fate progression.

Our data show that the maturation program caused by replication stress begins in S phase, consistent with recent studies suggesting that a number of critical cell fate transitions in somatic cells begin during S phase (Nakatani et al., 2022; Pop et al., 2010; Raz et al., 2021). S phase is a vulnerable period during which barriers to cell identity, such as inaccessible chromatin, repressive histone marks, or TF binding, might be more easily lowered by replication stress or alterations in replication fork speed

(Ramachandran et al., 2017; Šviković and Sale, 2017). During DNA replication, RNA polymerase and TFs are evicted ahead of the replication fork, and the inaccessibility of nascent DNA requires TFs to compete with newly deposited nucleosomes to rebind and reopen replicated chromatin (Bar-Ziv et al., 2020; Ramachandran and Henikoff, 2016; Stewart-Morgan et al., 2019). When considering that the pre-existing TF milieu specifies the differentiation program, that changes in gene expression are only accompanied by limited changes in chromatin accessibility, and that certain features of progenitor programs are also upregulated, it is conceivable that replication stress or slowed replication fork speed could alter the binding dynamics of lineage-specific TFs that are already expressed in the progenitor cell.

Histone marks must also be accurately re-established on daughter DNA. Recent studies have suggested that replication stress can alter the fidelity of histone recycling, including for parental histones carrying repressive marks (Clément et al., 2018; Escobar et al., 2019, 2021; Jasencakova et al., 2010), which could ultimately lead to epigenetic and gene expression changes (Papadopoulou et al., 2015). Intriguingly, loss of the CAF-1 histone chaperone, which associates with the sliding clamp PCNA and primarily deposits newly made histones, has been shown to facilitate cell fate changes in multiple systems (Cheloufi et al., 2015; Cheng et al., 2019; Franklin et al., 2022; Ishiuchi et al., 2015; Volk et al., 2018). In ER-Hoxa9 cells, the transcriptomic effects of CAF-1 knockdown appear to mirror those of BRQ treatment, although CAF-1 loss has also been shown to cause replication stress itself (Hoek and Stillman, 2003). Replication stress may also promote deposition of alternative histone variants with differential effects on DNA accessibility (Kim et al., 2018; Nakatani et al., 2022). How histone recycling might be altered by replication stress to support cell fate progression warrants further study.

Lastly, the chemical and genetic screen results suggest that multiple nodes in nucleotide biosynthesis and the replication machinery could be targeted as differentiation therapy (de Thé, 2018). Commonly used antimetabolites and chemotherapeutic agents, such as cisplatin and doxorubicin, can also induce replication stress and cell fate progression, yet these effects are likely to be masked by the cytotoxic doses to which cells are exposed and by limitations in our ability to determine cell fate *in vivo*. Moreover, unlike other tailored therapies such as retinoic acid in acute promyelocytic leukemia, replication stress inducers appear to be agnostic to the specific oncogenic driver or cell state, suggesting that such therapeutic strategies may be useful in settings that are less amenable to targeted approaches. However, replication stress is unable to suppress all oncogene-enforced progenitor programs, and a more comprehensive understanding of how replication stress modulates transcriptional state in different contexts is needed to develop combination strategies that alter cell fate for therapeutic benefit, including in settings outside of leukemia.

METHODS

Cell culture: Mouse Lys-GFP-ER-Hoxa9 ER-Hoxa9 cells were derived as described in Sykes et al. 2016. ER-Hoxa9 cells were grown in RPMI (Corning, 15-040-CV) with 10% dialyzed fetal bovine serum (Sigma, F0392), 4mM glutamine (Thermo Fisher; #25300164), and 1% penicillin/streptomycin (Corning, 45000-652), supplemented with 0.5 µM beta-estradiol (Sigma, E2758; made from a 10mM stock dissolved in 100% ethanol) and stem cell factor (SCF) from conditioned media generated from Chinese hamster ovary (CHO) cells that stably secrete SCF (Sykes et al., 2016; this conditioned media was added at 1% to achieve a final concentration of ~100 ng/ml). THP1, U937, and K562 cells were obtained from ATCC and grown in RPMI with 10% dialyzed fetal bovine serum (Gibco), 4mM glutamine, and 1% penicillin/streptomycin. Lenti-X 293T cells (ATCC) were grown in DMEM with 10% heat inactivated fetal bovine serum (Gibco) without antibiotics. All cell lines were regularly tested for mycoplasma.

Drugs: The following drugs were used: brequinar (Sigma-Aldrich; SML0113), teriflunomide (Sigma-Aldrich; SML0936), 6-azauridine (Sigma-Aldrich, A1882), pyrazofurin (Sigma-Aldrich; SML1502), 5-fluorouracil (Sigma-Aldrich; F6627), pyrimethamine (Cayman Chemical; #16472), cladribine (Cayman Chemical; #12085), 6-mercaptopurine (Sigma-Aldrich; #852678), 6-thioguanine (Cayman Chemical; #15774), mycophenolate mofetil (Sigma-Aldrich; SML0284), fulvestrant (Selleck Chemical; S1191), RX-3117 (MedChemExpress; HY-15228), hydroxyurea (Sigma-Aldrich; H8627), aphidicolin (Sigma-Aldrich; A0781), erastin (Sigma-Aldrich; E7781), rotenone (Selleck Chemical; S2348), diphenyleneiodonium chloride (Sigma-Aldrich; D2926), fenretinide (Cayman Chemical; #17688), 3-AP (ApexBio; C4564), gemcitabine (MedChemExpress; HY-17026), clofarabine (Sigma-Aldrich; C7495), phorbol 12-myristate 13-acetate (Sigma-Aldrich; P8139), etoposide (Sigma-Aldrich; E1383), cisplatin (Cayman Chemical; #13119), daunorubicin (Sigma-Aldrich; #30450), cytarabine (Selleck Chemical; S1648), neocarzinostatin (Sigma-Aldrich; N9162), VE-822 (Cayman Chemical; #24198), AZ20 (Selleck Chemical; S7050), AZD0156 (Selleck Chemical, S8375), rabusertib (Selleck Chemical; S2626), palbociclib (Selleck Chemical; S1116), and imatinib (Tocris; #5906). All drugs were stored at a stock concentration of 10 mM in DMSO at -20ºC except for hydroxyurea, which was stored at a stock concentration of 500 mM in water at -20ºC, and cisplatin, which was prepared fresh from powder prior to each use and diluted into DMF. The following nucleosides and nucleobases were used: adenine (Sigma-Aldrich; A8626), cytidine (Sigma-Aldrich; C4654), guanine (Sigma-Aldrich; G11950), guanosine (Sigma-Aldrich; G6752), uridine (Sigma-Aldrich; U3003), thymidine (Sigma-Aldrich; #89270). Adenine was prepared at 50 mM in 0.1 M NaOH and guanine was prepared at 25 mM in 0.1 M NaOH. Uridine, cytidine, and thymidine were made up at 100 mM in water. Guanosine was prepared at 100 mM in DMSO. All nucleoside and nucleobase stocks were stored at -20ºC.

Chemical screen: The Ludwig metabolic library has been described previously (Harris et al. 2019) and was screened in a 10-point 3X dilution series with the highest concentration screened at 10 µM at the ICCB Longwood Screening Facility at Harvard Medical School. The Lys-GFP-ER-Hoxa9 cells were diluted to a concentration of 75,000 cells per ml, and 200 µl was dispensed into 96-well round-bottom tissue-culture treated plates. 200 nl of each compound were transferred from the 384-well compound plates to the 96-well cell plates by robotic pinning. Brequinar at a final concentration of 2 µM was used as a positive control on every 96 well plate, and DMSO was used as a negative control. Two technical screening replicates were performed. After 4 days, cells were incubated with anti-CD11b-APC antibody (final concentration of 1:400; Clone M1/70, Biolegend), washed, and resuspended in FACS buffer with DAPI dye (Thermo). Cells were analyzed in 96-well format using an iQue3 (IntelliCyt).

Viability was determined using forward and side scatter profiles. Viability for each well was normalized to the average of the 72 DMSO-treated negative controls across the four 96 well plates corresponding to one 384-well compound source plate to determine a normalized percentage viability. Differentiation was determined by measuring APC and GFP fluorescence on DAPI-negative live cells. The percent differentiation was the percentage of live cells that fell in the APC positive, GFP positive flow quadrant. Initial data processing was performed using the ForeCyt 8 software (Sartorius). The AUC of viability and differentiation were calculated with in-house R scripts. Data were graphed using Prism GraphPad and least squares curve fit (log(inhibitor) vs response; variable slope four parameters). For the sensitization screen, we first classified drugs into those that increased or decreased differentiation compared to the BRQ control on the plate, then identified the least toxic dose where the percent of differentiated cells was less than 10 percent from the maximum effect.

Flow cytometry: Flow cytometry analysis was performed on BD FACSCanto, LSR II, and Celesta machines. For surface staining, the following antibodies were used at a 1:400 dilution: CD11b-APC (Biolegend; clone M1/70; #101211), CD14-FITC (BD; clone M5E2; #557153), CD16-FITC (BD; clone 3G8; #555406), CD235a-APC (Biolegend; clone HI264; #349114). Cells were washed once with PBS, then stained for 45 minutes on ice followed by a single wash with PBS and resuspension in PBS with 1 ng/ml DAPI.

For intracellular flow cytometry, the following antibodies were used at a 1:100 dilution: p-S345 Chk1 (Cell Signaling Technologies; clone 133D3; #2348) and p-S139 H2AX (Cell Signaling Technologies; clone 20D3; #9718). 100,000 cells were washed once with PBS, fixed for 10 minutes at room temperature with 20 µl 4% paraformaldehyde, then washed again and incubated at 4ºC for 30 minutes with primary antibody diluted in 1X Click-iT saponin-based permeabilization and wash reagent (Thermo Fisher, #C10419). Cells were then washed once with PBS with 1% BSA, then incubated at 4ºC for 30 minutes with goat anti-rabbit AF488 secondary antibody (Thermo Fisher; #A-11008) diluted at 1:1000 in the same saponin reagent, washed, and analyzed by flow cytometry.

For EdU incorporation experiments, the Click-iT Plus EdU Alexa Fluor 647 Flow Cytometry Assay Kit protocol (Thermo Fisher; #C10634) was used with minor modifications to the manufacturer's instructions. Briefly, 100,000 cells were pulsed with 20 µM EdU for 30 minutes prior to cell collection. After fixation, permeabilization was performed for 15 minutes with 25 µl of 1X permeabilization and wash reagent. A master mix was made with the following amounts of reagent per sample (added in order): 19.79 µl PBS, 0.83 µl copper protectant, 0.21 µl AF647 picolyl azide, and 4.16 µl reaction buffer. 25 µl of this master mix was then added to each sample of permeabilized cells, and the click reaction was allowed to proceed at room temperature for 30 minutes in the dark, washed once with PBS, and incubated with DAPI (0.1 µg/ml) or propidium iodide (CST #4087) at 4°C for 30 minutes prior to flow cytometry analysis.

Sorting was performed on BD FACSAria machines at the Koch Institute flow cytometry core, using the 70 µm nozzle. All cells were sorted into fresh cell culture media. Gating and downstream analysis were performed using FACSDiva (BD) software or using in-house scripts based on the FlowCytometryTools package in Python.

Cytospins: Cytospins were prepared as described in (Sykes et al., 2016). In brief, ER-Hoxa9 cells treated with various drugs were prepared in PBS at a concentration of 2 million/ml. Cytospin (Thermo Scientific Shandon) preparations were made (1,000 rpm for 60 seconds), and the cells were allowed to air dry. Cells were stained in 100% Wright-Giemsa stain (Siemens) for 2 min, then in 20% Wright-Giemsa diluted in PBS for 12 min. Stained cells were rinsed in deionized water, and coverslips were affixed with Permount prior to microscopy.

Immunofluorescence: For each experiment, 10,000 cells were allowed to adhere in each well of custom hydrophobic printed 30-well microscope slides using 0.1% poly-L-lysine, fixed with freshly made 4% paraformaldehyde (pH 7.2) for 10 minutes, washed 3 times with PBS, permeabilized with 0.2% triton-X in PBS for 20 minutes, washed 3 times with PBS, and blocked with 10% normal goat serum (Sigma) for 30 minutes. Samples were then incubated overnight with the following primary antibodies diluted in PBS with 0.1% Tween and 1% BSA: rabbit anti-mouse RPA2 (Abcam; ab76420; 1:50), rat anti-mouse RPA2 (CST; 2208S; 1:200), and rabbit anti-mouse γH2AX (CST; 9718; 1:1000). After 3 washes with PBS, samples were incubated for 1 hour with the following secondary antibodies, all at 1:1000 in PBS with 0.1% Tween and 1 ng/ml DAPI: goat anti-rabbit AF647 (Invitrogen; A-21245) and goat anti-rat AF647 (Invitrogen; A-21247), then washed 3 times with PBS and mounted using Fluoromount. Images were acquired on a DeltaVision Elite microscope platform (GE Healthcare Bio-Sciences) using the 60X Plan APO 1.42NA objective and a CoolSNAP HQ2 camera with 15 z-slices. Images were deconvoluted using constrained iterative deconvolution and stacks were collapsed using maximum intensity projection. Cells were identified and segmented using a semi-supervised approach, and foci and

19

intensities were automatically tabulated using ImageJ. For γH2AX and RPA foci in Figure 2, at least 300 cells were analyzed per condition. For RPA and γH2AX foci, at least 100 cells were analyzed per condition except for NCS, for which at least 50 cells were analyzed per condition. RPA coefficient of variation was calculated for each cell by dividing the standard deviation of RPA signal across each DAPI-positive region by its mean.

Mouse experiments: All experiments conducted in this study were approved by the Massachusetts General Hospital Institutional Animal Care and Use Committee (IACUC). For subcutaneous tumor growth, a maximum tumor burden of 1 cm^3 was permitted per IACUC protocol, and these limits were not exceeded. Female NU/J nude mice between 2 and 3 months old were used in this study. All animals were housed at ambient temperature and humidity (18–23□ºC, 40–60% humidity) with a 12h light and 12h dark cycle and co-housed with littermates with *ad libitum* access to water, unless otherwise stated. All experimental groups were age-matched, numbered and assigned based on treatment, and experiments were conducted in a blinded manner. Data were collected from distinct animals, where *n* represents biologically independent samples. Statistical methods were not used to predetermine sample size.

On the day of the experiment, 100 million THP-1 cells expressing pU6-sgNTC EF1Alpha-puro-T2A-BFP (to enable downstream analysis of tumor cells by flow cytometry) were washed and resuspended in 1 ml PBS, 1 ml Matrigel was added, and the cells were passed multiple times through an 18-gauge syringe to ensure a single cell suspension. 5 million cells (100 µl) were then injected subcutaneously into the right flank of each mouse. 13 days after cell injection, when palpable tumors had formed, animals were randomized and injected IP with either PEG or 50 mg/kg BRQ. Mice were weighed before the start of treatment to ensure that different cohorts had similar starting body weights, and body weights were also measured over the course of each experiment. Tumor volume was determined using $(W^2)(L)$, where *W* represents width and *L* represents length as measured by calipers. Four days after drug treatment, animals were euthanized and tumors were explanted. Tumors were dissociated by shaking for 30 minutes in a 37°C water bath in 5 ml of M199 media (Thermo Fisher 11150067) containing 1 mg/ml each of Collagenase Type 1 (Worthington Biochemical LS004216), Type 2 (Worthington Biochemical LS004204), Type 3 (Worthington Biochemical LS004216), and Type 4 (Worthington Biochemical LS004212), as well as 5 µl DNase I (Thermo Fisher #90083). 15 ml RPMI with 10% FBS was then added to stop the dissociation process, and cells were filtered using a 70 µm strainer and centrifuged at 500 g for 5 minutes. Red blood cells were lysed with 5 ml ACK lysis buffer (Quality Biological #118-156-721) for 7 minutes on ice, then 15 ml of RPMI with 10% FBS was added and cells were centrifuged and prepared for flow cytometry. BFP signal was used to gate for tumor cells.

Western blotting: The following primary antibodies were used, all at a dilution of 1:1000: p-S345 Chk1 (Cell Signaling Technologies #2348) Chk1 (Cell Signaling Technologies #2360), p-S139 H2AX (Cell Signaling Technologies #9718), CD11b (Novus; NB110-89474SS), tubulin (Abcam; ab4074), actin (Cell Signaling Technologies #8457), PU.1 (Cell Signaling Technologies #2258), and vinculin (Cell Signaling Technologies #13901). The following secondary antibodies were used: HRP-linked anti-rabbit IgG (Cell Signaling Technologies #7074, used at 1:5000) and HRP-linked anti-mouse IgG (Cell Signaling Technologies #7076, used at 1:2000). Briefly, cells were washed once with 10 ml ice-cold PBS, pelleted, lysed using LDS sample buffer (Invitrogen; NP0007) with 2% beta-mercaptoethanol (Sigma-Aldrich; M6250) at a concentration of 10 million cells/ml, loaded onto a Qiashredder column (Qiagen; #79656), and sheared by centrifugation at 21300 g for 30 seconds, and the eluate was boiled at 95ºC for 5 minutes. Samples were normalized using the Pierce 660 nm protein assay (Thermo Scientific; #22662) with the ionic detergent compatibility kit (Thermo Scientific; #22663) using BSA as a standard. Lysates were resolved by SDS-PAGE and proteins were transferred onto nitrocellulose or PVDF membranes using the iBlot2 Dry Blotting System (Thermo Fisher, IB21001, IB23001).

Metabolite profiling: After washing in blood bank saline, metabolites from 1 million cells were extracted in 1 ml ice-cold 80% methanol in water with 500 nM $^{13}C/^{15}N$-labeled amino acid standards (Cambridge Isotope Laboratories, Inc.). Cells were vortexed for 10 min at 4°C, and then centrifuged at maximum speed for 10 min at 4°C. Samples were dried under nitrogen gas and resuspended in 50/50 acetonitrile/water mixture.

Metabolites were measured using a Dionex UltiMate 3000 ultra-high performance liquid chromatography system connected to a Q Exactive benchtop Orbitrap mass spectrometer, equipped with an Ion Max source and a HESI II probe (Thermo Fisher Scientific). External mass calibration was performed using the standard calibration mixture every 7 days. Samples were separated by chromatography by injecting 2 µl of sample on a SeQuant ZIC-pHILIC Polymeric column (2.1 × 150 mm 5 µM, Millipore Sigma). Flow rate was set to 150 µl min, temperatures were set to 25°C for column compartment and 4°C for autosampler sample tray. Mobile Phase A consisted of 20 mM ammonium carbonate, 0.1% ammonium hydroxide. Mobile Phase B was 100% acetonitrile. The mobile phase gradient was as follows : 0–20 min.: linear gradient from 80% to 20% B; 20–20.5 min.: linear gradient from 20% to 80% B; 20.5–28 min.: hold at 80% B. Mobile phase was introduced into the ionization source set to the following parameters: sheath gas = 40, auxiliary gas = 15, sweep gas = 1, spray voltage = 3.1 kV, capillary temperature = 275°C, S-lens RF level = 40, probe temperature = 350°C. Metabolites were monitored in full-scan, polarity-switching, mode. An additional narrow range full-scan (220–700 m/z) in negative mode only was included to enhance nucleotide detection. The resolution was set at 70,000, the AGC target at 1×10^6 and the maximum injection time at 20 msec.

Relative quantitation of metabolites was performed with XCalibur QuanBrowser 2.2 (Thermo Fisher Scientific) using a 5 ppm mass tolerance and referencing an in-house retention time library of chemical standards. Raw peak areas of metabolites were normalized to cell number and then to the internal ^{13}C/^{15}N-labelled amino acid standards. In Figures S1B and S1C, metabolites are displayed if the variance of the log2 fold change values across all treatments (compared to control) is higher than 1.5.

Cell line generation: For all lentiviral transductions, lentiviral particles were generated by transfecting Lenti-X 293T cells (ATCC) with a 4:2:1:1 ratio of the target:pMDLg:pMD2.G:pRSV-REV plasmids using Transit 293T reagent (Mirus). After 48 hours, supernatant was clarified through a 0.45 µm PES filter and either snap frozen in liquid nitrogen and stored at -80ºC or added fresh to target cells. All cells were transduced using 250 µl viral supernatant and 250 µl cells at a concentration of 1e6/ml with polybrene (Millipore, TR-1003-G) added at a final concentration of 8 µg/ml.

To generate ER-Hoxa9 and THP-1 cell lines carrying dCas9, the plasmid pHR-UCOE-SFFV-dCas9-mCherry-ZIM3-KRAB (Addgene plasmid #154473) was transduced into cells as described above. Twenty-four hours after transduction, cells were centrifuged and resuspended in fresh media. After another twenty-four hours, cells within the top half of mCherry expression were single-cell sorted into four 96-well plates containing 75 µl conditioned media. Cell colonies were allowed to grow for 1-2 weeks, and viable colonies were screened for high mCherry expression and low baseline differentiation using flow cytometry.

To generate K562 cell lines carrying dCas9, cells were transduced with lentivirus generated from plasmid Addgene UCOE-SFFV-dCas9-BFP-KRAB (Addgene plasmid #85969) as described above. The top half of BFP+ cells was bulk sorted twice and then single cell cloned, and CRISPRi knockdown efficiency was validated using 3 benchmark guides (Palmer et al., 2018).

To generate CRISPRi knockdowns, sgRNA oligos were designed and cloned into the CRISPRi-v2 sgRNA plasmid pU6-sgRNA EF1Alpha-puro-T2A-BFP (Addgene plasmid #60955) using sequences from (Horlbeck et al., 2016). Oligos that were used are listed in Table S5. Lentivirus was generated as above and ER-Hoxa9 and THP-1 dCas9 lines were transduced with lentivirus for 24 hours. Subsequently, cells were recovered for 24 hours then selected using 2 µg/ml (ER-Hoxa9 cells) or 1 µg/ml (THP-1 cells) puromycin. Media was changed and fresh puromycin was added every 1-2 days to maintain selective pressure. After 4 days of selection, BFP positivity was assessed using flow cytometry (usually >97% BFP+). Note that for K562 cells whose dCas9 is fused to BFP, the BFP signal induced by the sgRNA plasmid is much stronger, allowing for unambiguous identification of sgRNA-carrying cells. Knockdown efficiency was tested using quantitative PCR, as described below.

To generate ER-Hoxa9 FUCCI cells, mCherry-Geminin (Sakaue-Sawano et al., 2008) was cloned into the pLV-Hygro vector (Addgene plasmid #85134), using Gibson cloning. Lentivirus was

generated and ER-Hoxa9 cells were transduced as above, then cells were sorted twice for the top half of mCherry-positive cells.

Quantitative PCR: Cells were treated as indicated, and 1 million cells were centrifuged, pelleted, and flash frozen in liquid nitrogen and placed at -80ºC. Pellets were processed in groups of 24 using the Zymo RNA Miniprep Kit, RNA was quantified using a Nanodrop, and 500 ng RNA was reverse transcribed into cDNA in a 10 µl reaction using the iScript cDNA synthesis kit (Bio-Rad). cDNA was then diluted 1:10 and 4 µl was used for quantitative RT-PCR using the LuminoCt SYBR Green master mix on a Roche LightCycler 480 machine. *RPS18* and *GAPDH*/*Gapdh* were used as expression controls where indicated. The primers used are listed in Table S5.

RNA-seq: The brequinar ER-Hoxa9 timecourse was performed as described in Sykes et al. 2016 and raw data for the E2 withdrawal ER-Hoxa9 timecourse were obtained from GSE84874 (Sykes et al., 2016). For all experiments, cells were treated as indicated (4 biological replicates per condition), then stained with a final concentration of 1 ng/ml DAPI in growth media, and 1 million live cells were sorted using a BD FACSAria and placed on ice. Immediately following the sort, cells were centrifuged, pelleted, and flash frozen in liquid nitrogen and placed at -80ºC. Pellets were processed in groups of 24 using the Zymo RNA Miniprep Kit and quantified using the Invitrogen Quant-it RNA kit. For all experiments not involving K562 cells, RNA was diluted to a concentration of 2 ng/µl and 5 µl of each sample was transferred to a 96 well plate, then poly-A enrichment and cDNA synthesis were performed in parallel as described (Soumillon et al., 2014), followed by library preparation using the Nextera XT kit and paired-end sequencing on an Illumina NextSeq 500. For K562 RNA-seq, RNA was diluted to a concentration of 10 ng/µl and 10 µl of each sample was transferred to a 96 well plate, then poly-A enrichment, cDNA synthesis, and library prep were performed in parallel using the Ultra II Directional RNA-Seq Kit (NEB E7760) and reads were sequenced 2x50bp on an Illumina NovaSeq S4.

Mouse and human data were mapped to mm10 and hg38 genomes, respectively, using STAR v2.7.8a and default parameters. Reads that mapped to transcripts were counted using featureCounts v2.0.1 (with parameters -M -O --fraction --primary). Normalization and differential gene expression analysis was performed using limma-voom (v3.4.6) on R. Gene ontology enrichment was performed using Enrichr.

CUT&RUN: ER-Hoxa9 and THP-1 cells were treated as indicated, then stained with a final concentration of 1 ng/ml DAPI in growth media, and 1 million live cells were sorted using a BD FACSAria and placed on ice. CUT&RUN was then performed using the Epicypher CUTANA CUT&RUN kit, using 500,000 cells for all experiments. The following antibodies were used (1 µl per 50 µl reaction): H3K4me1 (EMD Millipore #07-436), H3K4me3 (Epicypher #13-0028), ER (CST #8644), and IgG

(Epicypher #13-0041). Library construction was performed using the NEBNext Ultra II Library Preparation Kit following the manufacturer's protocol, and each library was indexed using NEBNext Multiplex Oligos for Illumina. For ER-Hoxa9, the library construction protocol was modified to generate shorter fragments as described in https://www.protocols.io/view/library-prep-for-cut-amp-run-with-nebnext-ultra-ii-wvgfe3w. Libraries were quantified using Qubit and Bioanalyzer and pooled for 2x40bp paired-end sequencing using an Illumina NextSeq 500. Mouse and human data were mapped to mm10 and hg38 genomes, respectively, using Bowtie2 v2.4.2 (with parameters --dovetail -I 10 -X 700 --very-sensitive-local --local), then normalized using the bamCoverage tool from deepTools (v3.5.0) (with parameters -bs 1 -e 200).

Samples were characterized in one of two ways. For ER-Hoxa9, peaks were called using SEACR (Meers et al., 2019). For H3K4me3, H3K4me1, and H3K27ac, counts were tabulated for each peak in the master ATAC-seq peak list (below), then normalized by library size and peak width to obtain a FPKM value for each peak. Motifs were identified using HOMER v4.11 (Heinz et al., 2010) and overlapping genes were identified using GREAT (McLean et al., 2010).

ATAC-seq: For THP-1 cells, cells were stained with a final concentration of 1 ng/ml DAPI in growth media, and 200,000 live cells were sorted using a BD FACSAria and placed on ice. 50,000 cells were then processed using the Active Motif ATAC-seq kit (cat. 53150). Libraries were constructed using the dual index barcodes included in the Active Motif ATAC-seq kit, except that after the PCR amplification, libraries were size selected with 1.5X SPRI beads (Beckman Coulter) instead of 1.2X SPRI beads in order to retain smaller fragments. Libraries were then quantified using Qubit and Bioanalyzer analysis, pooled, and sequenced using 2x40 paired-end sequencing on an Illumina NextSeq 500.

To generate ATAC-seq libraries for ER-Hoxa9 cells, 50,000 cells were used and libraries were constructed as previously described (Cheloufi et al., 2015; Corces et al., 2017). Briefly, cells were washed in PBS twice, counted and nuclei were isolated from 100,000 cells using 100 µl hypotonic buffer (10 mM Tris pH 7.4, 10 mM NaCl, 3 mM MgCl2, 0.1% NP40) to generate two independent transposition reactions. Nuclei were split in half and treated with 2.5 µl Tn5 Transposase (Illumina) for 30 minutes at 37°C. DNA from transposed nuclei was then isolated and PCR-amplified using barcoded Nextera primers (Illumina). Library QC was carried out using high sensitivity DNA bioanalyzer assay and Qubit measurement and sequenced using paired-end sequencing (PE50) on the Illumina HiSeq 2500 platform.

For data analysis, mouse and human data were trimmed using Cutadapt (v3.4) (with parameters -m 20 -q 20 -a CTGTCTCTTATA -A CTGTCTCTTATA), then aligned to the mm10 and hg38 genomes with Bowtie2 v2.4.2 (with parameters --dovetail -I 10 -X 1000 --very-sensitive). Reads in the mitochondrial genome and unannotated chromosomes as well as the UCSC blacklist were removed, then duplicates were removed with samtools markdup (v1.1.2), and the insert size distribution

24

was calculated using Picard CollectInsertSizeMetrics (v2.25.2) and validated to contain nucleosomal peaks. BED file was then constructed with each mate pair as a separate read using bedtools bamtobed (v2.3.0), and peaks were called using MACS2 callpeak (v2.2.7.1) (with parameters --nomodel --shift -100 --extsize 200 --keep-dup all --call-summits). Note that the MACS2 command shifts each read by 100 base pairs towards the 5' end and extends the read length to 200 base pairs, thus treating the 5' end of the original read (the Tn5 cut site) as the center of a new "fragment" that is then used for peak calling and other downstream analysis. To normalize tracks for visualization, reads overlapping shared peaks were counted for each BAM file using featureCounts (with parameters -M -O) and normalization factors were calculated from these counts using the calcNormFactors function in the edgeR package (v3.32.1) in R. Visualization was performed using the bedGraphToBigWig utility and the igv-jupyter package in Python.

To identify changes in motif accessibility, ChromVAR (Schep et al., 2017) was used. For downstream analysis, peaks from all samples from the same experiment were merged as follows. Peak summits (called using MACS2) were extended by 25bp in each direction, then only peaks that were present in both replicates for each condition (overlapping by at least 50%) were retained. Peak lists were then merged across samples, merging peaks that were within 50bp of each other. ATAC-seq and CUT&RUN reads were then counted against this master peak list using featureCounts (-p -O -M --fraction). Differential ATAC-seq peaks were calculated using edgeR with a log2 fold change threshold of 1.5 and an adjusted p-value of 0.05. Peaks were annotated to genomic features using ChIPseeker (Yu et al., 2015), where promoters were defined as the region between 2000bp upstream of the TSS and 500bp downstream of the TSS.

To assess concordance between ATAC-seq and gene expression, the master peak list was subsetted to only include peaks that exceeded the 25th percentile ATAC-seq and H3K4me1 CUT&RUN signal (for ER-Hoxa9) or H3K27ac signal (for THP-1) in at least one timepoint. GREAT was then run on this set of peaks in single-gene mode, assigning peaks to the single closest transcriptional start site within 100kb. High-complexity genes were defined as those whose number of associated peaks was in the top tertile (Kiani et al., 2022). Shared upregulated or downregulated genes were considered to be high-complexity genes with a log2 fold change in expression > 1 or < -1, and peaks were considered to be more accessible if their log2 fold change in ATAC-seq signal was >0.5 compared to baseline (other thresholds are shown in the supplementary figure). As alternative metrics of gene accessibility, we also took the median log2 fold change in accessibility for all peaks assigned to a given gene, or calculated a variant of the ABC score (Fulco et al., 2019) by weighting each peak's log fold change in accessibility by the inverse of its distance from the TSS, then adding up weighted scores for all peaks assigned to a given gene.

MULTI-seq: For BRQ treatments, 1 million cells were washed twice with PBS and treated with 2 μM BRQ for 6, 12, 24, or 48h. For estrogen withdrawal, 1 million cells were washed twice with PBS and then resuspended in media without estrogen for 6, 12, 24, or 48h. To barcode each sample, MULTI-seq (McGinnis et al. 2019) was used; the barcode for each sample is included in the supplementary files. The anchor and co-anchor lipid-modified oligos were a gift from Zev Gartner. Briefly, for each condition, 400,000 cells were rinsed twice in PBS and resuspended in 180 μl PBS. 20 μl of a 10X stock of anchor:barcode (per sample: 0.88 μl anchor, 0.44 μl 100 μM barcode, and 20.7 μl PBS) was added to each sample, pipetted gently to mix, and incubated on ice for 5 minutes. Next, 20 μl of a 10X stock of coanchor (per sample: 0.88 μl co-anchor and 21.2 μl PBS) was added to each sample, pipetted gently to mix, and incubated on ice for 5 minutes. 700 μl ice cold 1% BSA in PBS was then added to each sample, and cells were centrifuged at 4°C for 5 minutes. The supernatant was aspirated and the wash was repeated 2X with ice cold BSA in PBS. After the last wash, cells were resuspended in 300 μl PBS/BSA, filtered through a cell strainer, and counted using a Nexcelom cell counter. Cells were adjusted to a concentration of 1 million/ml using ice cold BSA in PBS, and 50 μl of each sample was pooled into one tube and placed on ice. Cells were then loaded into the 10X Genomics microfluidics chip for processing and scRNAseq. 28,500 cells were loaded in order to obtain enough data for 15,000 usable cells (calculation performed at https://satijalab.org/costpercell/).

Library construction proceeded as indicated in the 10X Genomics scRNAseq v3 protocol except as follows (adapted from McGinnis et al. 2019). During cDNA amplification, 1 μl of a 2.5 μM MULTI-seq primer (5'-CTTGGCACCCGAGAATTCC-3') was added to the master mix. After the 0.6X SPRI clean-up, the supernatant was saved for barcode extraction rather than discarded. To the 60 μl supernatant, 260 μl SPRI beads and 180 μl 100% isopropanol were added for a final ratio of 1.8X beads, pipetted up and down 10x, and incubated at room temperature for 5 minutes. The tube was then placed on a magnetic rack for 5 minutes, supernatant discarded, beads washed 2x with 500 μl 80% ethanol, and eluted with 50 μl buffer EB. This SPRI purification step was repeated once more to further purify the barcode fraction. The barcode fraction was quantified using Qubit, and then library preparation PCR was performed using the Kapa HiFi HotStart ReadyMix with 3.5 ng barcode DNA, 2.5 μl 10 μM universal i5 primer, and 2.5 μl 10 μM TruSeq RPI1 primer in a 50 μl reaction for 8-12 cycles. The PCR product was purified using a final SPRI bead concentration of 1.6X, eluted, and quantified on a Bioanalyzer; a peak between 175 and 200bp was expected. The barcode library was mixed 1:10 with the transcript library and sequenced on an Illumina NextSeq 500.

For data analysis, FASTQ files were mapped to the mouse cDNA and intronic transcriptomes with the 10x v3 whitelist (all files available at https://github.com/pachterlab/MBGBLHGP_2019/releases) using Kallisto v0.4.6. Samples were then demultiplexed using the deMULTIplex package (v1.0.2) in R (https://github.com/chris-mcginnis-ucsf/MULTI-seq) and doublets were discarded (McGinnis et al., 2019). Spliced and unspliced read data were analyzed using scVelo (Bergen et al., 2020). Briefly, raw

data were filtered for genes that had at least 20 counts across all samples and cells that had at least 5000 reads mapping to spliced RNAs. To calculate a granulocyte score, z-scores were summed for the following genes: *Spi1*, *Clec4d*, *Tyrobp*, *Csf2rb*, *Mpo*, *Fcer1g*, *Fcgr3*, *Slpi*, and *Sell*. To plot cells around a cell cycle, PCA was performed using S and G2/M genes from Seurat, and a UMAP was then plotted using this reduced representation.

CRISPRi screen: The CRISPRi screen was performed using THP-1 dCas9 cells generated as above and a genome-wide library with 10 sgRNAs per gene (Addgene #1000000090) as described in (Palmer et al., 2018) with the following modifications. Briefly, the library was electroporated into MegaX cells (Invitrogen #C640003) and plasmid was maxiprepped (Qiagen) and sequenced as described below to ensure even representation of guides. THP-1 cells were always maintained between 250,000 and 1 million cells/ml, and two biological replicates were performed starting at the lentiviral infection step. 200 million cells were infected for 24 hours with lentivirus at an MOI between 0.25 and 0.35 with 8 µg/ml polybrene. Lentiviral media was then replaced with fresh media, and 24 hours later, 1 µg/ml puromycin was added to select library-containing cells. Media was exchanged and fresh puromycin was added 24 and 48 hours afterwards. Four days after puromycin treatment, viability was >90% and BFP positivity was >97% for both replicates, indicating that the selection was complete. At this point, puromycin was removed and 200 million cells were treated with 500 nM brequinar. 48 hours later, cells were concentrated to 20 million cells/ml in fresh media, and at least 15 million cells from both the top and bottom 25% of CD11b expression were sorted using a BD FACSAria, pelleted, and frozen at -80ºC for later processing.

To obtain amplicons for sequencing, genomic DNA from each cell pellet was extracted using the Machery Nagel Nucleospin Blood L kit following the manufacturer's instructions except with an overnight incubation at 70C and elution of DNA into 200 µl 10mM Tris (pH 8.5). Guides were then PCR amplified using a universal i7 primer and custom i5 primers indexed for each sample, with reactions split such that each 50 µl PCR reaction contained no more than 2.5µg DNA in a 20 µl volume. Most pellets were split across either 16 or 32 PCR reactions depending on cell number. PCR was performed using the NEBNext Ultra Q5 2X Master Mix with the following cycling parameters: initial denaturation at 98°C for 2 minutes, then 24 cycles of denaturation at 98°C for 15 seconds and annealing/extension at 65°C for 75 seconds, then a final extension of 65°C for 5 minutes. All reactions for each pellet were pooled, and successful amplification was verified by running 10 µl of the PCR on an agarose gel to obtain an expected band between 250 and 260bp. 200 µl of the PCR reaction (roughly corresponding to 1µg of amplicon) was then purified using a double-sided selection with AMpure XP beads (Beckman Coulter). First, to remove genomic DNA, 0.5X volume of beads (100 µl) was added to the PCR reaction, mixed well, and incubated at room temperature for 10 minutes, and beads were placed on a magnet and supernatant was saved. Second, to remove primer dimers, 135 µl beads were added to

290 μl of supernatant (final bead volume of 1.2X), mixed well, and incubated at room temperature for 10 minutes, and beads were placed on a magnet and supernatant was discarded. DNA was then eluted from the beads using 20 μl of 0.1X TE (pH 8.5), quantified using Qubit and Bioanalyzer, and pooled for 1x75 sequencing on an Illumina NextSeq 500 using an equimolar mix of custom read 1 primers (p5_seq_primer, listed in Table S5).

For data analysis, FASTQ files were demultiplexed and barcode sequences were matched to the master list of CRISPRi barcodes. Only perfect matches were retained. Viability for each guide in the presence of brequinar was calculated by calculating a counts per million (CPM) value for each guide relative to the total library size in each sample, dividing the sum of CPMs from the CD11b up and down fractions by the CPM from the plasmid library, then taking its z-score relative to all other guides. Guide scores were calculated by taking the log2 ratio of CPMs between the CD11b-high and CD11b-low fraction for each guide, and the median score across all 10 guides for each gene was used as the gene score. Gene interactions were plotted for the top 500 scoring genes using STRING and Cytoscape, and GO annotations were calculated using Metascape.

Perturb-seq analysis: We normalized and filtered cells and combined all cells for a given knockdown into a "pseudobulk" transcriptome (Replogle et al., 2022). To identify knockdowns that led to discordant transcriptomes when compared to non-targeting control knockdowns, PCA was performed on all pseudobulk transcriptomes for the top 2000 highest variable genes (by expression), and 15 PCs were retained because the coefficient of variation for nontargeting transcriptomes did not decrease significantly with more PCs. Using this 15-dimensional space, Euclidean distance between each knockdown transcriptome and the median of non-targeting transcriptomes was calculated, and knockdowns were kept if their distance was higher than the mean + 2 standard deviations of the non-targeting distances. PCA was then recalculated using this set of 514 non-targeting transcriptomes and 2,297 divergent targeting transcriptomes, and a UMAP was plotted using the top 30 PCs. Replication stress-related genes were identified by taking the intersection of genes from GO ontology #0006261 (DNA-templated DNA replication), GO #0045005 (DNA-templated DNA replication maintenance of fidelity), GO #1903932 (regulation of DNA primase activity), Reactome #R-HSA-905320 (nucleotide biosynthesis), and Wikipathway #4022 (pyrimidine biosynthesis), and genes whose symbols started with "POLR", "PELO", or "PNPT1" were removed because they were unrelated to DNA replication. Myeloid scores were calculated by summing z-scores for the following genes: *CSF3R*, *LST1*, *CD33*, *LYZ*, *AIF1*, *CD55*, and *SPI1*. Erythrocyte scores were similarly calculated using the following genes: *HBG1*, *GYPA*, *ERMAP*, *ALAS2*, *HBA1*, *KLF1*, and *SLC25A37*.

Data and code availability: All sequencing data generated in this study are deposited on GEO under accession number GSEXXXXXX. All code is available on GitHub at https://github.com/bdo311/hsu_do_2022.

ACKNOWLEDGEMENTS

AUTHOR CONTRIBUTIONS

P.P.H., B.T.D., and M.G.V.H. conceived of the project. P.P.H. conducted chemical screens with the help of N.A. and I.S.H. P.P.H., B.T.D., S.Y.V., and Z.W. conducted the majority of experiments in the paper. B.T.D. and S.Y.V. conducted CRISPRi screens with the help of K.L.A., S.B., and A.M.D. B.T.D., S.Y.V., and R.F. performed computational analysis. C.C. provided reagents and assisted with CRISPRi screen design. X.A.S. generated the FUCCI construct. D.R.S. conducted irradiation experiments. T.H. and J.M. conducted *in vivo* experiments. S.C. and D.B.S. performed the RNA-seq and ATAC-seq timecourse in ER-Hoxa9 cells. J.M.R. and J.S.W. provided Perturb-seq data and expertise. P.P.H. and B.T.D. wrote the paper with input from M.G.V.H. and all co-authors. D.B.S. and M.G.V.H. obtained funding.

FUNDING

CONFLICTS OF INTEREST

D.B.S. is a co-founder and holds equity in Clear Creek Bio and is a consultant and holds equity in SAFI Biosolutions. M.G.V.H. discloses that he is on the scientific advisory board of Agios Pharmaceuticals, iTeos Therapeutics, Drioa Ventures, Sage Therapeutics, and Auron Therapeutics. P.P.H. has consulted for Auron Therapeutics. J.S.W. serves as an advisor to and/or has equity in KSQ Therapeutics, Maze Therapeutics, and 5AM Ventures, all unrelated to the present work. J.M.R. consults for Maze Therapeutics and Waypoint Bio. All other authors declare that they have no conflict of interest.

REFERENCES

Alabert, C., Barth, T.K., Reverón-Gómez, N., Sidoli, S., Schmidt, A., Jensen, O.N., Imhof, A., and Groth, A. (2015). Two distinct modes for propagation of histone PTMs across the cell cycle. Genes Dev. *29*, 585. https://doi.org/10.1101/gad.256354.114.

Alvarez, S., Díaz, M., Flach, J., Rodriguez-Acebes, S., López-Contreras, A.J., Martínez, D., Cañamero, M., Fernández-Capetillo, O., Isern, J., Passegué, E., et al. (2015). Replication stress caused by low MCM expression limits fetal erythropoiesis and hematopoietic stem cell functionality. Nat. Commun. *6*. https://doi.org/10.1038/ncomms9548.

An, X., Schulz, V.P., Li, J., Wu, K., Liu, J., Xue, F., Hu, J., Mohandas, N., and Gallagher, P.G. (2014). Global transcriptome analyses of human and murine terminal erythroid differentiation. Blood *123*, 3466–3477. https://doi.org/10.1182/blood-2014-01-548305.

Atashpaz, S., Samadi Shams, S., Gonzalez, J.M., Sebestyén, E., Arghavanifard, N., Gnocchi, A., Albers, E., Minardi, S., Faga, G., Soffientini, P., et al. (2020). ATR expands embryonic stem cell fate potential in response to replication stress. ELife *9*, e54756. https://doi.org/10.7554/eLife.54756.

Baksh, S.C., and Finley, L.W.S. (2020). Metabolic Coordination of Cell Fate by α-Ketoglutarate-Dependent Dioxygenases. Trends Cell Biol. *0.* https://doi.org/10.1016/j.tcb.2020.09.010.

Baksh, S.C., and Finley, L.W.S. (2021). Metabolic Coordination of Cell Fate by α-Ketoglutarate-Dependent Dioxygenases. Trends Cell Biol. *31*, 24–36. https://doi.org/10.1016/j.tcb.2020.09.010.

Bar-Ziv, R., Brodsky, S., Chapal, M., and Barkai, N. (2020). Transcription Factor Binding to Replicated DNA. Cell Rep. *30*, 3989-3995.e4. https://doi.org/10.1016/j.celrep.2020.02.114.

Bergen, V., Lange, M., Peidli, S., Wolf, F.A., and Theis, F.J. (2020). Generalizing RNA velocity to transient cell states through dynamical modeling. Nat. Biotechnol. *38*, 1408–1414. https://doi.org/10.1038/s41587-020-0591-3.

Birsoy, K., Wang, T., Chen, W.W., Freinkman, E., Abu-Remaileh, M., and Sabatini, D.M. (2015). An Essential Role of the Mitochondrial Electron Transport Chain in Cell Proliferation Is to Enable Aspartate Synthesis. Cell *162*, 540–551. https://doi.org/10.1016/j.cell.2015.07.016.

Brignole, E.J., Tsai, K.-L., Chittuluru, J., Li, H., Aye, Y., Penczek, P.A., Stubbe, J., Drennan, C.L., and Asturias, F. (2018). 3.3-Å resolution cryo-EM structure of human ribonucleotide reductase with substrate and allosteric regulators bound. ELife *7*, e31502. https://doi.org/10.7554/eLife.31502.

Caielli, S., Cardenas, J., de Jesus, A.A., Baisch, J., Walters, L., Blanck, J.P., Balasubramanian, P., Stagnar, C., Ohouo, M., Hong, S., et al. (2021). Erythroid mitochondrial retention triggers myeloid-dependent type I interferon in human SLE. Cell *184,* 4464-4479.e19. https://doi.org/10.1016/j.cell.2021.07.021.

Carey, B.W., Finley, L.W.S., Cross, J.R., Allis, C.D., and Thompson, C.B. (2015). Intracellular α-ketoglutarate maintains the pluripotency of embryonic stem cells. Nature *518,* 413–416. https://doi.org/10.1038/nature13981.

Cheloufi, S., Elling, U., Hopfgartner, B., Jung, Y.L., Murn, J., Ninova, M., Hubmann, M., Badeaux, A.I., Euong Ang, C., Tenen, D., et al. (2015). The histone chaperone CAF-1 safeguards somatic cell identity. Nature *528*, 218–224. https://doi.org/10.1038/nature15749.

Cheng, L., Zhang, X., Wang, Y., Gan, H., Xu, X., Lv, X., Hua, X., Que, J., Ordog, T., and Zhang, Z. (2019). Chromatin Assembly Factor 1 (CAF-1) facilitates the establishment of facultative heterochromatin during pluripotency exit. Nucleic Acids Res. *47*, 11114–11131. https://doi.org/10.1093/nar/gkz858.

Christian, S., Merz, C., Evans, L., Gradl, S., Seidel, H., Friberg, A., Eheim, A., Lejeune, P., Brzezinka, K., Zimmermann, K., et al. (2019). The novel dihydroorotate dehydrogenase (DHODH) inhibitor BAY 2402234 triggers differentiation and is effective in the treatment of myeloid malignancies. Leukemia *33*, 2403–2415. https://doi.org/10.1038/s41375-019-0461-5.

Clément, C., Orsi, G.A., Gatto, A., Boyarchuk, E., Forest, A., Hajj, B., Miné-Hattab, J., Garnier, M., Gurard-Levin, Z.A., Quivy, J.-P., et al. (2018). High-resolution visualization of H3 variants during replication reveals their controlled recycling. Nat. Commun. *9*, 1–17. https://doi.org/10.1038/s41467-018-05697-1.

Collins, C.T., and Hess, J.L. (2016). Role of HOXA9 in leukemia: dysregulation, cofactors and essential targets. Oncogene *35*, 1090–1098. https://doi.org/10.1038/onc.2015.174.

Corces, M.R., Trevino, A.E., Hamilton, E.G., Greenside, P.G., Sinnott-Armstrong, N.A., Vesuna, S., Satpathy, A.T., Rubin, A.J., Montine, K.S., Wu, B., et al. (2017). An improved ATAC-seq protocol reduces background and enables interrogation of frozen tissues. Nat. Methods *14*, 959–962. https://doi.org/10.1038/nmeth.4396.

Daigneault, M., Preston, J.A., Marriott, H.M., Whyte, M.K.B., and Dockrell, D.H. (2010). The Identification of Markers of Macrophage Differentiation in PMA-Stimulated THP-1 Cells and Monocyte-Derived Macrophages. PLOS ONE *5*, e8668. https://doi.org/10.1371/journal.pone.0008668.

Dalton, S., and Coverdell, P.D. (2015). Linking the cell cycle to cell fate decisions. Trends Cell Biol. *25*, 592–600. https://doi.org/10.1016/j.tcb.2015.07.007.

Dembitz, V., Tomic, B., Kodvanj, I., Simon, J.A., Bedalov, A., and Visnjic, D. (2019). The ribonucleoside AICAr induces differentiation of myeloid leukemia by activating the ATR/Chk1 kinase via pyrimidine depletion. J. Biol. Chem. jbc.RA119.009396. https://doi.org/10.1074/jbc.RA119.009396.

Diehl, F.F., Miettinen, T.P., Elbashir, R., Nabel, C.S., Manalis, S.R., Lewis, C.A., and Heiden, M.G.V. (2021). Nucleotide imbalance decouples cell growth from cell proliferation. 2021.12.06.471399. https://doi.org/10.1101/2021.12.06.471399.

Döhner, H., Estey, E., Grimwade, D., Amadori, S., Appelbaum, F.R., Büchner, T., Dombret, H., Ebert, B.L., Fenaux, P., Larson, R.A., et al. (2017). Diagnosis and management of AML in adults: 2017 ELN recommendations from an international expert panel. Blood *129*, 424–447. https://doi.org/10.1182/blood-2016-08-733196.

Dwivedi, V.K., Pardo-Pastor, C., Droste, R., Kong, J.N., Tucker, N., Denning, D.P., Rosenblatt, J., and Horvitz, H.R. (2021). Replication stress promotes cell elimination by extrusion. Nature 1–6. https://doi.org/10.1038/s41586-021-03526-y.

Ebert, P.S. (1976). Erythroid Differentiation in Cultured Friend Leukemia Cells Treated with Metabolic Inhibitors. 5. .

Emmanuel, N., Ragunathan, S., Shan, Q., Wang, F., Giannakou, A., Huser, N., Jin, G., Myers, J., Abraham, R.T., and Unsal-Kacmaz, K. (2017). Purine Nucleotide Availability Regulates mTORC1 Activity through the Rheb GTPase. Cell Rep. *19*, 2665–2680. https://doi.org/10.1016/j.celrep.2017.05.043.

Escobar, T.M., Oksuz, O., Saldaña-Meyer, R., Descostes, N., Bonasio, R., and Reinberg, D. (2019). Active and Repressed Chromatin Domains Exhibit Distinct Nucleosome Segregation during DNA Replication. Cell *179*, 953-963.e11. https://doi.org/10.1016/j.cell.2019.10.009.

Escobar, T.M., Yu, J.-R., Liu, S., Lucero, K., Vasilyev, N., Nudler, E., and Reinberg, D. (2021). Inheritance of Repressed Chromatin Domains during S-phase Requires the Histone Chaperone NPM1 (Molecular Biology).

Faust, N., Varas, F., Kelly, L.M., Heck, S., and Graf, T. (2000). Insertion of enhanced green fluorescent protein into the lysozyme gene creates mice with green fluorescent granulocytes and macrophages. Blood *96*, 719–726. .

Forey, R., Poveda, A., Sharma, S., Barthe, A., Padioleau, I., Renard, C., Lambert, R., Skrzypczak, M., Ginalski, K., Lengronne, A., et al. (2020). Mec1 Is Activated at the Onset of Normal S Phase by Low-dNTP Pools Impeding DNA Replication. Mol. Cell *78*, 396-410.e4. https://doi.org/10.1016/j.molcel.2020.02.021.

Franklin, R., Guo, Y., He, S., Chen, M., Ji, F., Zhou, X., Frankhouser, D., Do, B.T., Chiem, C., Jang, M., et al. (2022). Regulation of chromatin accessibility by the histone chaperone CAF-1 sustains lineage fidelity. Nat. Commun. *13*, 2350. https://doi.org/10.1038/s41467-022-29730-6.

Fulco, C.P., Nasser, J., Jones, T.R., Munson, G., Bergman, D.T., Subramanian, V., Grossman, S.R., Anyoha, R., Patwardhan, T.A., Nguyen, T.H., et al. (2019). Activity-by-Contact model of enhancer specificity from thousands of CRISPR perturbations. BioRxiv 529990. https://doi.org/10.1101/529990.

van Galen, P., Hovestadt, V., Wadsworth II, M.H., Hughes, T.K., Griffin, G.K., Battaglia, S., Verga, J.A., Stephansky, J., Pastika, T.J., Lombardi Story, J., et al. (2019). Single-Cell RNA-Seq Reveals AML Hierarchies Relevant to Disease Progression and Immunity. Cell *176*, 1265-1281.e24. https://doi.org/10.1016/j.cell.2019.01.031.

Gonzalez-Menendez, P., Romano, M., Yan, H., Deshmukh, R., Papoin, J., Oburoglu, L., Daumur, M., Dumé, A.-S., Phadke, I., Mongellaz, C., et al. (2021). An IDH1-vitamin C crosstalk drives human erythroid development by inhibiting pro-oxidant mitochondrial metabolism. Cell Rep. *34*, 108723. https://doi.org/10.1016/j.celrep.2021.108723.

Griffin, J., Munroe, D., Major, P., and Kufe, D. (1982). Induction of differentiation of human myeloid leukemia cells by inhibitors of DNA synthesis. Exp. Hematol. *10*, 774–781. .

Grow, E.J., Weaver, B.D., Smith, C.M., Guo, J., Stein, P., Shadle, S.C., Hendrickson, P.G., Johnson, N.E., Butterfield, R.J., Menafra, R., et al. (2021). p53 convergently activates Dux/DUX4 in embryonic stem cells and in facioscapulohumeral muscular dystrophy cell models. Nat. Genet. *53*, 1207–1220. https://doi.org/10.1038/s41588-021-00893-0.

Guan, H.-H., Huang, Y.-H., Lin, E.-S., Chen, C.-J., and Huang, C.-Y. (2021). Plumbagin, a Natural Product with Potent Anticancer Activities, Binds to and Inhibits Dihydroorotase, a Key Enzyme in Pyrimidine Biosynthesis. Int. J. Mol. Sci. *22*, 6861. https://doi.org/10.3390/ijms22136861.

Gusella, J.F., and Housman, D. (1976). Induction of erythroid differentiation in vitro by purines and purine analogues. Cell *8*, 263–269. https://doi.org/10.1016/0092-8674(76)90010-6.

Harris, I.S., Endress, J.E., Coloff, J.L., Selfors, L.M., McBrayer, S.K., Rosenbluth, J.M., Takahashi, N., Dhakal, S., Koduri, V., Oser, M.G., et al. (2019). Deubiquitinases Maintain Protein Homeostasis and Survival of Cancer Cells upon Glutathione Depletion. Cell Metab. *29*, 1166-1181.e6. https://doi.org/10.1016/j.cmet.2019.01.020.

Heinz, S., Benner, C., Spann, N., Bertolino, E., Lin, Y.C., Laslo, P., Cheng, J.X., Murre, C., Singh, H., and Glass, C.K. (2010). Simple combinations of lineage-determining transcription factors prime cis-regulatory elements required for macrophage and B cell identities. Mol. Cell *38*, 576–589. https://doi.org/10.1016/j.molcel.2010.05.004.

Hoek, M., and Stillman, B. (2003). Chromatin assembly factor 1 is essential and couples chromatin assembly to DNA replication in vivo. Proc. Natl. Acad. Sci. U. S. A. *100*, 12183–12188. https://doi.org/10.1073/pnas.1635158100.

Horlbeck, M.A., Gilbert, L.A., Villalta, J.E., Adamson, B., Pak, R.A., Chen, Y., Fields, A.P., Park, C.Y., Corn, J.E., Kampmann, M., et al. (2016). Compact and highly active next-generation libraries for CRISPR-mediated gene repression and activation. ELife *5*, e19760. https://doi.org/10.7554/eLife.19760.

Hoxhaj, G., Hughes-Hallett, J., Timson, R.C., Ilagan, E., Yuan, M., Asara, J.M., Ben-Sahra, I., and Manning, B.D. (2017). The mTORC1 Signaling Network Senses Changes in Cellular Purine Nucleotide Levels. Cell Rep. *21*, 1331–1346. https://doi.org/10.1016/j.celrep.2017.10.029.

Huang, M., Wang, Y., Collins, M., and Graves, L.M. (2004). CPEC induces erythroid differentiation of human myeloid leukemia K562 cells through CTP depletion and p38 MAP kinase. Leukemia *18*, 1857–1863. https://doi.org/10.1038/sj.leu.2403490.

Ibarra, A., Schwob, E., and Méndez, J. (2008). Excess MCM proteins protect human cells from replicative stress by licensing backup origins of replication. Proc. Natl. Acad. Sci. *105*, 8956–8961. https://doi.org/10.1073/pnas.0803978105.

Inomata, K., Aoto, T., Binh, N.T., Okamoto, N., Tanimura, S., Wakayama, T., Iseki, S., Hara, E., Masunaga, T., Shimizu, H., et al. (2009). Genotoxic Stress Abrogates Renewal of Melanocyte Stem Cells by Triggering Their Differentiation. Cell *137*, 1088–1099. https://doi.org/10.1016/j.cell.2009.03.037.

Intlekofer, A.M., and Finley, L.W.S. (2019). Metabolic signatures of cancer cells and stem cells. Nat. Metab. *1*, 177–188. https://doi.org/10.1038/s42255-019-0032-0.

Ishiuchi, T., Enriquez-Gasca, R., Mizutani, E., Bošković, A., Ziegler-Birling, C., Rodriguez-Terrones, D., Wakayama, T., Vaquerizas, J.M., and Torres-Padilla, M.-E. (2015). Early embryonic-like cells are induced by downregulating replication-dependent chromatin assembly. Nat. Struct. Mol. Biol. *22*, 662–671. https://doi.org/10.1038/nsmb.3066.

Jasencakova, Z., Scharf, A.N.D., Ask, K., Corpet, A., Imhof, A., Almouzni, G., and Groth, A. (2010). Replication stress interferes with histone recycling and predeposition marking of new histones. Mol. Cell *37*, 736–743. https://doi.org/10.1016/j.molcel.2010.01.033.

Kato, T., Liu, N., Morinaga, H., Asakawa, K., Muraguchi, T., Muroyama, Y., Shimokawa, M., Matsumura, H., Nishimori, Y., Tan, L.J., et al. (2021). Dynamic stem cell selection safeguards the genomic integrity of the epidermis. Dev. Cell *56*, 3309-3320.e5. https://doi.org/10.1016/j.devcel.2021.11.018.

Kensler, T.W., Jayaram, H.N., and Cooney, D.A. (1982). Effects of acivicin and PALA, singly and in combination, on de novo pyrimidine biosynthesis. Adv. Enzyme Regul. *20*, 57–73. https://doi.org/10.1016/0065-2571(82)90008-5.

Kiani, K., Sanford, E.M., Goyal, Y., and Raj, A. (2022). Changes in chromatin accessibility are not concordant with transcriptional changes for single-factor perturbations. 2022.02.03.478981. https://doi.org/10.1101/2022.02.03.478981.

Kim, J., Sturgill, D., Sebastian, R., Khurana, S., Tran, A.D., Edwards, G.B., Kruswick, A., Burkett, S., Hosogane, E.K., Hannon, W.W., et al. (2018). Replication Stress Shapes a Protective Chromatin Environment across Fragile Genomic Regions. Mol. Cell *69*, 36-47.e7. https://doi.org/10.1016/j.molcel.2017.11.021.

Klein, K.N., Zhao, P.A., Lyu, X., Sasaki, T., Bartlett, D.A., Singh, A.M., Tasan, I., Zhang, M., Watts, L.P., Hiraga, S., et al. (2021). Replication timing maintains the global epigenetic state in human cells. Science *372*, 371–378. https://doi.org/10.1126/science.aba5545.

Kueh, H.Y., Champhekar, A., Nutt, S.L., Elowitz, M.B., and Rothenberg, E.V. (2013). Positive Feedback Between PU.1 and the Cell Cycle Controls Myeloid Differentiation. Science *341*, 670–673. https://doi.org/10.1126/science.1240831.

Le Magnen, C., Shen, M.M., and Abate-Shen, C. (2018). Lineage Plasticity in Cancer Progression and Treatment. Annu. Rev. Cancer Biol. *2*, 271–289. https://doi.org/10.1146/annurev-cancerbio-030617-050224.

Lehman, H.K., and Segal, B.H. (2020). The role of neutrophils in host defense and disease. J. Allergy Clin. Immunol. *145*, 1535–1544. https://doi.org/10.1016/j.jaci.2020.02.038.

Lin, B., Srikanth, P., Castle, A.C., Nigwekar, S., Malhotra, R., Galloway, J.L., Sykes, D.B., and Rajagopal, J. (2018). Modulating Cell Fate as a Therapeutic Strategy. Cell Stem Cell *23*, 329–341. https://doi.org/10.1016/j.stem.2018.05.009.

Liu, C., Konagaya, Y., Chung, M., Daigh, L.H., Fan, Y., Yang, H.W., Terai, K., Matsuda, M., and Meyer, T. (2020). Altered G1 signaling order and commitment point in cells proliferating without CDK4/6 activity. Nat. Commun. *11*, 5305. https://doi.org/10.1038/s41467-020-18966-9.

Ludwig, L.S., Lareau, C.A., Bao, E.L., Nandakumar, S.K., Muus, C., Ulirsch, J.C., Chowdhary, K., Buenrostro, J.D., Mohandas, N., An, X., et al. (2019). Transcriptional States and Chromatin Accessibility Underlying Human Erythropoiesis. Cell Rep. *27*, 3228-3240.e7. https://doi.org/10.1016/j.celrep.2019.05.046.

Ma, S., Zhang, B., LaFave, L.M., Earl, A.S., Chiang, Z., Hu, Y., Ding, J., Brack, A., Kartha, V.K., Tay, T., et al. (2020). Chromatin Potential Identified by Shared Single-Cell Profiling of RNA and Chromatin. Cell *183*, 1103-1116.e20. https://doi.org/10.1016/j.cell.2020.09.056.

McGinnis, C.S., Patterson, D.M., Winkler, J., Conrad, D.N., Hein, M.Y., Srivastava, V., Hu, J.L., Murrow, L.M., Weissman, J.S., Werb, Z., et al. (2019). MULTI-seq: sample multiplexing for single-cell RNA sequencing using lipid-tagged indices. Nat. Methods *16*, 619–626. https://doi.org/10.1038/s41592-019-0433-8.

McKenzie, M.D., Ghisi, M., Oxley, E.P., Ngo, S., Cimmino, L., Esnault, C., Liu, R., Salmon, J.M., Bell, C.C., Ahmed, N., et al. (2019). Interconversion between Tumorigenic and Differentiated States in Acute Myeloid Leukemia. Cell Stem Cell 25, 258-272.e9. https://doi.org/10.1016/j.stem.2019.07.001.

McLean, C.Y., Bristor, D., Hiller, M., Clarke, S.L., Schaar, B.T., Lowe, C.B., Wenger, A.M., and Bejerano, G. (2010). GREAT improves functional interpretation of cis-regulatory regions. Nat. Biotechnol. 28, 495–501. https://doi.org/10.1038/nbt.1630.

Meers, M.P., Tenenbaum, D., and Henikoff, S. (2019). Peak calling by Sparse Enrichment Analysis for CUT&RUN chromatin profiling. Epigenetics Chromatin 12, 42. https://doi.org/10.1186/s13072-019-0287-4.

Meier, J.L. (2013). Metabolic Mechanisms of Epigenetic Regulation. ACS Chem. Biol. 8, 2607–2621. https://doi.org/10.1021/cb400689r.

Molinuevo, R., Freije, A., Contreras, L., Sanz, J.R., and Gandarillas, A. (2020). The DNA damage response links human squamous proliferation with differentiation. J. Cell Biol. 219. https://doi.org/10.1083/jcb.202001063.

Muench, D.E., Olsson, A., Ferchen, K., Pham, G., Serafin, R.A., Chutipongtanate, S., Dwivedi, P., Song, B., Hay, S., Chetal, K., et al. (2020). Mouse models of neutropenia reveal progenitor-stage-specific defects. Nature 1–6. https://doi.org/10.1038/s41586-020-2227-7.

Nakano, H., Minami, I., Braas, D., Pappoe, H., Wu, X., Sagadevan, A., Vergnes, L., Fu, K., Morselli, M., Dunham, C., et al. (2017). Glucose inhibits cardiac muscle maturation through nucleotide biosynthesis. ELife 6, e29330. https://doi.org/10.7554/eLife.29330.

Nakatani, T., Lin, J., Ji, F., Ettinger, A., Pontabry, J., Tokoro, M., Altamirano-Pacheco, L., Fiorentino, J., Mahammadov, E., Hatano, Y., et al. (2022). DNA replication fork speed underlies cell fate changes and promotes reprogramming. Nat. Genet. 1–10. https://doi.org/10.1038/s41588-022-01023-0.

Nathan, D.G. (1985). Regulation of Fetal Hemoglobin Synthesis in the Hemoglobinopathies. Ann. N. Y. Acad. Sci. 445, 177–187. https://doi.org/10.1111/j.1749-6632.1985.tb17187.x.

Oburoglu, L., Tardito, S., Fritz, V., de Barros, S.C., Merida, P., Craveiro, M., Mamede, J., Cretenet, G., Mongellaz, C., An, X., et al. (2014). Glucose and Glutamine Metabolism Regulate Human Hematopoietic Stem Cell Lineage Specification. Cell Stem Cell 15, 169–184. https://doi.org/10.1016/j.stem.2014.06.002.

Palmer, A.C., Chidley, C., and Sorger, P.K. (2018). A curative combination therapy for lymphomas achieves high fractional cell killing through low cross-resistance and drug additivity but not synergy (Cancer Biology).

Papadopoulou, C., Guilbaud, G., Schiavone, D., and Sale, J.E. (2015). Nucleotide Pool Depletion Induces G-Quadruplex-Dependent Perturbation of Gene Expression. Cell Rep. *13*, 2491–2503. https://doi.org/10.1016/j.celrep.2015.11.039.

Papaemmanuil, E., Gerstung, M., Bullinger, L., Gaidzik, V.I., Paschka, P., Roberts, N.D., Potter, N.E., Heuser, M., Thol, F., Bolli, N., et al. (2016). Genomic Classification and Prognosis in Acute Myeloid Leukemia. N. Engl. J. Med. *374*, 2209–2221. https://doi.org/10.1056/NEJMoa1516192.

Park, J.-I., Choi, H.-S., Jeong, J.-S., Han, J.-Y., and Kim, I.-H. (2001). Involvement of p38 Kinase in Hydroxyurea-induced Differentiation of K562 Cells. Cell Growth Differ. *12*, 481–486. .

Paul, F., Arkin, Y., Giladi, A., Jaitin, D.A., Kenigsberg, E., Keren-Shaul, H., Winter, D., Lara-Astiaso, D., Gury, M., Weiner, A., et al. (2015). Transcriptional Heterogeneity and Lineage Commitment in Myeloid Progenitors. Cell *163*, 1663–1677. https://doi.org/10.1016/j.cell.2015.11.013.

Perrimon, N., Pitsouli, C., and Shilo, B.-Z. (2012). Signaling Mechanisms Controlling Cell Fate and Embryonic Patterning. Cold Spring Harb. Perspect. Biol. *4*, a005975. https://doi.org/10.1101/cshperspect.a005975.

Pession, A., Martino, V., Tonelli, R., Beltramini, C., Locatelli, F., Biserni, G., Franzoni, M., Freccero, F., Montemurro, L., Pattacini, L., et al. (2003). MLL-AF9 oncogene expression affects cell growth but not terminal differentiation and is downregulated during monocyte-macrophage maturation in AML-M5 THP-1 cells. Oncogene *22*, 8671–8676. https://doi.org/10.1038/sj.onc.1207125.

Phanstiel, D.H., Van Bortle, K., Spacek, D.V., Hess, G.T., Shamim, M.S., Machol, I., Love, M.I., Aiden, E.L., Bassik, M.C., and Snyder, M.P. (2017). Static And Dynamic DNA Loops Form AP-1 Bound Activation Hubs During Macrophage Development. BioRxiv 142026+. https://doi.org/10.1101/142026.

Pop, R., Shearstone, J.R., Shen, Q., Liu, Y., Hallstrom, K., Koulnis, M., Gribnau, J., and Socolovsky, M. (2010). A Key Commitment Step in Erythropoiesis Is Synchronized with the Cell Cycle Clock through Mutual Inhibition between PU.1 and S-Phase Progression. PLOS Biol. *8*, e1000484. https://doi.org/10.1371/journal.pbio.1000484.

Quintanal-Villalonga, Á., Chan, J.M., Yu, H.A., Pe'er, D., Sawyers, C.L., Sen, T., and Rudin, C.M. (2020). Lineage plasticity in cancer: a shared pathway of therapeutic resistance. Nat. Rev. Clin. Oncol. *17*, 360–371. https://doi.org/10.1038/s41571-020-0340-z.

Ramachandran, S., and Henikoff, S. (2016). Transcriptional Regulators Compete with Nucleosomes Post-replication. Cell *165*, 580–592. https://doi.org/10.1016/j.cell.2016.02.062.

Ramachandran, S., Ahmad, K., and Henikoff, S. (2017). Capitalizing on disaster: Establishing chromatin specificity behind the replication fork. BioEssays *39*, 1600150. https://doi.org/10.1002/bies.201600150.

Raz, A.A., Wurtzel, O., and Reddien, P.W. (2021). Planarian stem cells specify fate yet retain potency during the cell cycle. Cell Stem Cell *0*. https://doi.org/10.1016/j.stem.2021.03.021.

Rencricca, N.J., Morse, B.S., Monette, F.C., Howard, D., and Stohlman, F. (1975). Hydroxyurea-induced erythroid differentiation. Proc. Soc. Exp. Biol. Med. Soc. Exp. Biol. Med. N. Y. N *149*, 1052–1054. https://doi.org/10.3181/00379727-149-38956.

Replogle, J.M., Saunders, R.A., Pogson, A.N., Hussmann, J.A., Lenail, A., Guna, A., Mascibroda, L., Wagner, E.J., Adelman, K., Lithwick-Yanai, G., et al. (2022). Mapping information-rich genotype-phenotype landscapes with genome-scale Perturb-seq. Cell *185*, 2559-2575.e28. https://doi.org/10.1016/j.cell.2022.05.013.

Reverón-Gómez, N., González-Aguilera, C., Stewart-Morgan, K.R., Petryk, N., Flury, V., Graziano, S., Johansen, J.V., Jakobsen, J.S., Alabert, C., and Groth, A. (2018). Accurate Recycling of Parental Histones Reproduces the Histone Modification Landscape during DNA Replication. Mol. Cell *72*, 239-249.e5. https://doi.org/10.1016/j.molcel.2018.08.010.

Roy, N., and Hebrok, M. (2015). Regulation of cellular identity in cancer. Dev. Cell *35*, 674–684. https://doi.org/10.1016/j.devcel.2015.12.001.

Rubin, A.J., Barajas, B.C., Furlan-Magaril, M., Lopez-Pajares, V., Mumbach, M.R., Howard, I., Kim, D.S., Boxer, L.D., Cairns, J., Spivakov, M., et al. (2017). Lineage-specific dynamic and pre-established enhancer–promoter contacts cooperate in terminal differentiation. Nat. Genet. *49*, 1522. https://doi.org/10.1038/ng.3935.

Sakaue-Sawano, A., Kurokawa, H., Morimura, T., Hanyu, A., Hama, H., Osawa, H., Kashiwagi, S., Fukami, K., Miyata, T., Miyoshi, H., et al. (2008). Visualizing Spatiotemporal Dynamics of Multicellular Cell-Cycle Progression. Cell *132*, 487–498. https://doi.org/10.1016/j.cell.2007.12.033.

Santos, M.A., Faryabi, R.B., Ergen, A.V., Day, A.M., Malhowski, A., Canela, A., Onozawa, M., Lee, J.-E., Callen, E., Gutierrez-Martinez, P., et al. (2014). DNA-damage-induced differentiation of leukaemic cells as an anti-cancer barrier. Nature *514*, 107–111. https://doi.org/10.1038/nature13483.

Saxena, S., and Zou, L. (2022). Hallmarks of DNA replication stress. Mol. Cell *82*, 2298–2314. https://doi.org/10.1016/j.molcel.2022.05.004.

Schep, A.N., Wu, B., Buenrostro, J.D., and Greenleaf, W.J. (2017). chromVAR: inferring transcription-factor-associated accessibility from single-cell epigenomic data. Nat. Methods *14*, 975–978. https://doi.org/10.1038/nmeth.4401.

Schwartz, A.J., Goyert, J.W., Solanki, S., Kerk, S.A., Chen, B., Castillo, C., Hsu, P.P., Do, B.T., Singhal, R., Dame, M.K., et al. (2021). Hepcidin sequesters iron to sustain nucleotide metabolism and mitochondrial function in colorectal cancer epithelial cells. Nat. Metab. 1–14. https://doi.org/10.1038/s42255-021-00406-7.

Shapira, S.N., and Christofk, H.R. (2020). Metabolic Regulation of Tissue Stem Cells. Trends Cell Biol. *30*, 566–576. https://doi.org/10.1016/j.tcb.2020.04.004.

Sharpley, M.S., Chi, F., Hoeve, J.T., and Banerjee, U. (2021). Metabolic plasticity drives development during mammalian embryogenesis. Dev. Cell *56*, 2329-2347.e6. https://doi.org/10.1016/j.devcel.2021.07.020.

Sherman, M.H., Kuraishy, A.I., Deshpande, C., Hong, J.S., Cacalano, N.A., Gatti, R.A., Manis, J.P., Damore, M.A., Pellegrini, M., and Teitell, M.A. (2010). AID-Induced Genotoxic Stress Promotes B Cell Differentiation in the Germinal Center via ATM and LKB1 Signaling. Mol. Cell *39*, 873–885. https://doi.org/10.1016/j.molcel.2010.08.019.

Solmonson, A., Faubert, B., Gu, W., Rao, A., Cowdin, M.A., Menendez-Montes, I., Kelekar, S., Rogers, T.J., Pan, C., Guevara, G., et al. (2022). Compartmentalized metabolism supports midgestation mammalian development. Nature *604*, 349–353. https://doi.org/10.1038/s41586-022-04557-9.

Soumillon, M., Cacchiarelli, D., Semrau, S., Oudenaarden, A. van, and Mikkelsen, T.S. (2014). Characterization of directed differentiation by high-throughput single-cell RNA-Seq. 003236. https://doi.org/10.1101/003236.

Stewart-Morgan, K.R., Reverón-Gómez, N., and Groth, A. (2019). Transcription Restart Establishes Chromatin Accessibility after DNA Replication. Mol. Cell *75*, 284-297.e6. https://doi.org/10.1016/j.molcel.2019.04.033.

Sui, L., Xin, Y., Du, Q., Georgieva, D., Diedenhofen, G., Haataja, L., Su, Q., Zuccaro, M.V., Kim, J., Fu, J., et al. (2021). Reduced replication fork speed promotes pancreatic endocrine differentiation and controls graft size. JCI Insight https://doi.org/10.1172/jci.insight.141553.

Sullivan, L.B., Gui, D.Y., Hosios, A.M., Bush, L.N., Freinkman, E., and Vander Heiden, M.G. (2015). Supporting Aspartate Biosynthesis Is an Essential Function of Respiration in Proliferating Cells. Cell *162*, 552–563. .

Sutherland, J.A., Turner, A.R., Mannoni, P., McGann, L.E., and Turc, J.M. (1986). Differentiation of K562 leukemia cells along erythroid, macrophage, and megakaryocyte lineages. J. Biol. Response Mod. *5*, 250–262. .

Šviković, S., and Sale, J.E. (2017). The Effects of Replication Stress on S Phase Histone Management and Epigenetic Memory. J. Mol. Biol. *429*, 2011–2029. https://doi.org/10.1016/j.jmb.2016.11.011.

Sykes, D.B., Kfoury, Y.S., Mercier, F.E., Wawer, M.J., Law, J.M., Haynes, M.K., Lewis, T.A., Schajnovitz, A., Jain, E., Lee, D., et al. (2016). Inhibition of Dihydroorotate Dehydrogenase Overcomes Differentiation Blockade in Acute Myeloid Leukemia. Cell *167*, 171-186.e15. https://doi.org/10.1016/J.CELL.2016.08.057.

Takagi, M., Uno, H., Nishi, R., Sugimoto, M., Hasegawa, S., Piao, J., Ihara, N., Kanai, S., Kakei, S., Tamura, Y., et al. (2015). ATM Regulates Adipocyte Differentiation and Contributes to Glucose Homeostasis. Cell Rep. *10*, 957–967. https://doi.org/10.1016/j.celrep.2015.01.027.

TeSlaa, T., Chaikovsky, A.C., Lipchina, I., Escobar, S.L., Hochedlinger, K., Huang, J., Graeber, T.G., Braas, D., and Teitell, M.A. (2016). α-Ketoglutarate Accelerates the Initial Differentiation of Primed Human Pluripotent Stem Cells. Cell Metab. *24*, 485–493. https://doi.org/10.1016/j.cmet.2016.07.002.

de Thé, H. (2018). Differentiation therapy revisited. Nat. Rev. Cancer *18*, 117–127. https://doi.org/10.1038/nrc.2017.103.

Toledo, L.I., Altmeyer, M., Rask, M.-B., Lukas, C., Larsen, D.H., Povlsen, L.K., Bekker-Jensen, S., Mailand, N., Bartek, J., and Lukas, J. (2013). ATR Prohibits Replication Catastrophe by Preventing Global Exhaustion of RPA. Cell *155*, 1088–1103. https://doi.org/10.1016/j.cell.2013.10.043.

Tomic, B., Smoljo, T., Lalic, H., Dembitz, V., Batinic, J., Batinic, D., Bedalov, A., and Visnjic, D. (2022). Cytarabine-induced differentiation of AML cells depends on Chk1 activation and shares the mechanism with inhibitors of DHODH and pyrimidine synthesis. Sci. Rep. *12*, 11344. https://doi.org/10.1038/s41598-022-15520-z.

Uchida, N., Haro-Mora, J.J., Demirci, S., Fujita, A., Raines, L., Hsieh, M.M., and Tisdale, J.F. (2018). High-level embryonic globin production with efficient erythroid differentiation from a K562 erythroleukemia cell line. Exp. Hematol. *62*, 7-16.e1. https://doi.org/10.1016/j.exphem.2018.02.007.

Volk, A., Liang, K., Suraneni, P., Li, X., Zhao, J., Bulic, M., Marshall, S., Pulakanti, K., Malinge, S., Taub, J., et al. (2018). A CHAF1B-Dependent Molecular Switch in Hematopoiesis and Leukemia Pathogenesis. Cancer Cell *34*, 707-723.e7. https://doi.org/10.1016/j.ccell.2018.10.004.

Wang, E., Zhou, H., Nadorp, B., Cayanan, G., Chen, X., Yeaton, A.H., Nomikou, S., Witkowski, M.T., Narang, S., Kloetgen, A., et al. (2021). Surface antigen-guided CRISPR screens identify regulators of myeloid leukemia differentiation. Cell Stem Cell *28*, 718-731.e6. https://doi.org/10.1016/j.stem.2020.12.005.

Wang, J., Sun, Q., Morita, Y., Jiang, H., Groß, A., Lechel, A., Hildner, K., Guachalla, L.M., Gompf, A., Hartmann, D., et al. (2012). A Differentiation Checkpoint Limits Hematopoietic Stem Cell Self-Renewal in Response to DNA Damage. Cell *148*, 1001–1014. https://doi.org/10.1016/j.cell.2012.01.040.

Xie, X., Shi, Q., Wu, P., Zhang, X., Kambara, H., Su, J., Yu, H., Park, S.-Y., Guo, R., Ren, Q., et al. (2020). Single-cell transcriptome profiling reveals neutrophil heterogeneity in homeostasis and infection. Nat. Immunol. *21*, 1119–1133. https://doi.org/10.1038/s41590-020-0736-z.

Yu, G., Wang, L.-G., and He, Q.-Y. (2015). ChIPseeker: an R/Bioconductor package for ChIP peak annotation, comparison and visualization. Bioinformatics *31*, 2382–2383. https://doi.org/10.1093/bioinformatics/btv145.

Zalc, A., Sinha, R., Gulati, G.S., Wesche, D.J., Daszczuk, P., Swigut, T., Weissman, I.L., and Wysocka, J. (2021). Reactivation of the pluripotency program precedes formation of the cranial neural crest. Science *371*. https://doi.org/10.1126/science.abb4776.

Zee, B.M., Poels, K.E., Yao, C.-H., Kawabata, K.C., Wu, G., Duy, C., Jacobus, W.D., Senior, E., Endress, J.E., Jambhekar, A., et al. (2021). Combined epigenetic and metabolic treatments overcome differentiation blockade in acute myeloid leukemia. IScience *24*, 102651. https://doi.org/10.1016/j.isci.2021.102651.

Zeman, M.K., and Cimprich, K.A. (2014). Causes and consequences of replication stress. Nat. Cell Biol. *16*, 2–9. https://doi.org/10.1038/ncb2897.

Zhao, L., Ye, P., and Gonda, T.J. (2014). The MYB proto-oncogene suppresses monocytic differentiation of acute myeloid leukemia cells via transcriptional activation of its target gene GFI1. Oncogene *33*, 4442–4449. https://doi.org/10.1038/onc.2013.419.

(2009). The transcriptional network that controls growth arrest and differentiation in a human myeloid leukemia cell line. Nat. Genet. *41*, 553–562. https://doi.org/10.1038/ng.375.

FIGURE LEGENDS

Figure 1. A focused pharmacologic screen reveals molecules targeting nucleotide metabolism can promote leukemia differentiation.

A. Schematic of mouse ER-Hoxa9 granulocyte-monocyte progenitor (GMP) system (Sykes et al., 2016). Treatment with brequinar (BRQ) and withdrawal of estrogen (-E2) to suppress ER-Hoxa9 activity are known inducers of differentiation towards the neutrophil state, and the neutrophil markers CD11b and Lysozyme-GFP can be monitored to assess the extent of lineage progression. A screen was performed for other metabolic perturbations that could induce differentiation.

B. Plot showing area under the curve (AUC) for CD11b/GFP expression (differentiation) and viability for ER-Hoxa9 cells in response to all drugs in the metabolic drug library (Harris et al., 2019). Cells were treated for 4 days with ten doses of each drug up to 10 µM (see Methods).

C. Percent viability (blue) and differentiation as assessed by CD11b and GFP expression (red) for ER-Hoxa9 GMP cells treated with each of the indicated drugs. Data from two technical screening replicates are plotted. The enzyme target of each drug is color coded as indicated. DHODH, dihydroorotate dehydrogenase. CTPS, cytidine triphosphate synthetase. UMPS, uridine monophosphate synthetase. TYMS, thymidylate synthetase. DHFR, dihydrofolate reductase. IMPDH, inosine monophosphate dehydrogenase.

D. Area under the curve (AUC) for CD11b/GFP expression (differentiation) for each drug in the metabolic drug screen, grouped by category of drug target. P-values were calculated using a Mann-Whitney U test for each category compared to the distribution of all AUC values.

E. Log2 fold change in levels of NTPs and dNTPs in ER-Hoxa9 GMP cells following 24h of treatment with the indicated drug (all at 1 µM), with or without rescue by addition of the indicated cognate nucleotides (all at 1 mM). Log fold change values are compared to the median of the untreated normalized area under the peak. Some metabolites were not detected due to low abundance. BRQ, brequinar. U, uridine. PYR, pyrazofurin. LTX, lometrexol. MMF, mycophenolate mofetil. Hx, hypoxanthine. G, guanine. U, uridine. (*), p < 0.05; (**), p < 0.005, and p-values were calculated using a t-test on log fold change values for each treatment compared to DMSO treatment (denoted to the left of the bars), or for each treatment-rescue pair (denoted to the right of the bars).

F. Percentage of CD11b-expressing ER-Hoxa9 GMP cells following 96h of treatment with the indicated purine synthesis inhibitors (LTX at 41 nM, MMF at 370 nM) or pyrimidine synthesis inhibitors (BRQ at 1.1 µM, RX-3117 at 1.1 µM, PYR at 123 nM), with or without addition of cognate nucleotides (all at 1 mM). p < 0.05, (**), p < 0.005, or as indicated, and p-values were calculated using a t-test on samples with and without nucleotides. Abbreviations are as in (E).

G. Percentage of CD11b-expressing ER-Hoxa9 GMP cells following addition of increasing concentrations of adenine (A), guanine (G), thymidine (T), cytidine (C), or uridine (U) for 96 hours. The highest concentration depicted is 1 mM with a 3-fold lower dilution for each lower concentration.

H. Percent viability (blue) and differentiation, as assessed by CD11b or CD16 expression (red or green), for THP-1 and U937 human AML cells following treatment with the indicated concentration of BRQ for 96 hours.

I. Percent viability (blue) and differentiation, as assessed by CD235a expression (green), for K562 human erythroleukemia cells following treatment with the indicated concentration of BRQ for 72 hours.

Figure 2. Replication stress links nucleotide depletion to differentiation.

A. Percent viability (blue) and differentiation, as assessed by CD11b and GFP expression (green), for ER-Hoxa9 cells after treatment with the indicated doses of HU or APH for 96 hours (n=2).

B. Log fold change of intracellular levels of dATP, dCTP, or TTP (top) and ATP, CTP, GTP, or UTP (bottom) in ER-Hoxa9 following 24h of treatment with DMSO, 1 µM BRQ, 50 µM HU, or 1 µM APH (n=4). (ns) not significant, (*) p < 0.05, (**) p < 0.005, (***) p < 0.0005, and (****) p < 0.00005, and adjusted p-values were calculated using a two-way ANOVA with the Šidák correction for multiple comparisons.

C. Representative flow cytometry plots (EdU-AF647 vs. DAPI) in ER-Hoxa9 cells cultured in DMSO, 1 µM BRQ, 50 µM HU, or 1 µM APH for 4 hours then pulsed with EdU for the last 30 minutes.

D. Median fluorescence intensity (MFI) of EdU incorporation during S phase in ER-Hoxa9 cells cultured in DMSO, 1 µM BRQ, 50 µM HU, or 1 µM APH for 4 hours (n=3-4). (***) $p < 0.0005$, (****) $p < 0.00005$, and p-values were calculated using a one-way ANOVA with Dunnett's multiple comparisons test.

E. Immunofluorescence images of ER-Hoxa9 cells treated with DMSO, 1 µM BRQ, or 25 µM HU for 24h then stained for DAPI (blue), RPA (yellow), and γH2AX (green). Scale bars represent 10 µm.

F. Number of γH2AX foci, number of RPA foci, and RPA coefficient of variation per cell after treatment of ER-Hoxa9 cells with DMSO, 1 µM BRQ, or 25 µM HU for 24h. (****) $p < 0.00005$, Mann-Whitney U test.

G. Schematic showing experiment to assess response to brequinar in AML cells in mice. Five million THP-1 cells expressing BFP were injected subcutaneously into the flanks of nude mice, and once tumors formed a measurable size (~11 days) mice were treated with vehicle (PEG) or 50 mg/kg BRQ IP for 3 days, followed by tumor harvest and analysis of BFP+ cells by flow cytometry.

H. Assessment of tumor size before and after vehicle (PEG) or BRQ treatment (n=4). P values from Student's two sample t-test.

I. Percentage of CD11b+ CD14-, CD11b+ CD14+, or CD11b- CD14+ THP-1 cells in tumors as assessed by flow cytometry (n=4). P values from Student's two sample t-test.

J. Percentage of pChk1-positive THP-1 cells in tumors as assessed by flow cytometry (n=4). P values from Student's two sample t-test.

K. Percentage of γH2AX-positive THP-1 cells in tumors as assessed by flow cytometry (n=4). P values from Student's two sample t-test.

Figure 3. Genetic screens demonstrate that depletion of proteins involved in DNA replication can drive differentiation.

A. Schematic of CRISPRi screen to assess modulators of BRQ-induced CD11b induction in THP-1 cells.

B. Scatterplot showing results of screen ranked by gene score (Z-score of the enrichment of each knockdown in the top versus bottom quartile of CD11b expression), colored in black for the top hits and red for selected genes involved in nucleotide metabolism, DNA replication, and DNA repair. Data are merged from two biological replicates (see Figure S3A).

C. Enriched gene ontology categories from various ontologies summarized by Metascape and plotted by -log10(q-value) (y-axis) for the top 500 hits. All categories have a fold enrichment of at

least 10 and at least 10 (top hits) genes in the hit list. GO terms related to DNA replication and DNA repair are highlighted in red.

D. Mean fluorescence intensity (MFI) of EdU incorporation during S phase in single-gene knockdown THP-1 cell lines treated with DMSO or 500 nM BRQ for 48 hours (n=3). (*) $p < 0.05$, (**) $p < 0.005$, (***) $p < 0.0005$, Student's two-sample t-test.

E. Gene set enrichment analysis for RNA-seq data from THP-1 dCas9-KRAB cells transduced with sgMCM2, sgPOLD3, sgGOT2, and sgABCB7 compared to control sgNTC, using upregulated genes from PMA-treated THP-1 cells compared to untreated cells as the gene set of interest. NES, normalized enrichment score.

F. Schematic of genome-wide Perturb-seq experiment in K562 cells reported in (Replogle et al. 2022).

G. Scatterplot of knockdowns scored by the strength of an induced myeloid or erythroid signature (see STAR Methods). Replication- and nucleotide synthesis-related genes are highlighted in red. Horizontal and vertical dotted lines represent the 99th percentile score. Inset is displayed for clarity.

H. Metascape enrichment for genes whose knockdowns lead to top 50 erythroid (top) or myeloid (bottom) scores.

I. Scatterplot of erythroid score in K562 cells (calculated as in G) versus CD11b+ score in THP-1 cells (from Figure 3B). Replication- and nucleotide synthesis-related genes are highlighted in red.

Figure 4. Replication stress drives differentiation during S phase and is independent of the replication stress response.

A. (Top left) Schematic showing ER-Hoxa9 Geminin-mCherry cells that express mCherry during S/G2 and GFP as a differentiation marker. (Top right) Representative flow cytometry plots (20,000 cells) of cells treated with 1 µM BRQ for different amounts of time. (Bottom) Fold change in the percentage of GFP+ cells in G1 or S/G2 phases after treatment with DMSO, 1 µM BRQ, 50 µM HU, or 10 µM FULV for different amounts of time. All values are normalized to the median percentage of GFP+ cells in G1 or S/G2 phases at the start of the experiment. (ns) not significant, (*) $p < 0.05$, (**) $p < 0.005$, (***) $p < 0.0005$, and (****) $p < 0.00005$, and adjusted p-values were calculated using a two-way ANOVA with the Šidák correction for multiple comparisons. BRQ, brequinar. HU, hydroxyurea. FULV, fulvestrant.

B. (Left) Flow cytometry plots assessing EdU incorporation versus DNA content (DAPI) for ER-Hoxa9 treated with DMSO for 24 hours or BRQ for 16, 20, or 24 hours, with CD11b+ cells colored in red. (Right) Quantification of the percentage of CD11b+ cells in S phase for cells treated with DMSO, BRQ, or HU for 0, 16, 20, or 24 hours (n=3). (***) $p < 0.0005$, (****) $p < 0.00005$, (ns) $p > 0.05$, and p-values are calculated using a Student's t-test compared to all data values for DMSO treatment.

C. Relative scRNAseq expression of *Ung* (a G1 marker), *Rrm2* (S phase), and *Aurka* (G2/M phase), scaled from 0 to 1, for ER-Hoxa9 cells treated with 1 μM BRQ (top) or estrogen withdrawal (-E2, bottom) for 0, 12, 24, and 48 hours. Cells are plotted in UMAP space calculated from a principal components analysis conducted using only cell cycle-related genes.

D. Granulocyte score for BRQ-treated (top) or E2 withdrawn (bottom) cells treated at 0, 12, 24, and 48h, plotted in the same coordinates as in (C).

E. Percentage of ER-Hoxa9 cells in each cell cycle phase after 24h of growth in media with 100 ng/ml or 2 ng/ml SCF as determined by flow cytometry.

F. Percentage of CD11b-expressing ER-Hoxa9 cells following 48h of treatment with DMSO, 1 μM BRQ, or 10 μM FULV in 100 or 2 ng/ml SCF media.

G. Single-guide CD11b scores for negative control guides or knockdown of *ITGAM* (CD11b; negative control), *KAT2A* (a gene whose knockdown induces significant differentiation), *ATR*, *ATM*, *CDKN1A*, *CHEK1*, *and CHEK2* in THP-1 dCas9-KRAB-mCherry cells from the CRISPRi screen in Figure 3A. P-values were calculated using the Mann-Whitney U test compared to scores for negative control guides.

H. Percentage of CD11b-expressing ER-Hoxa9 cells following 24h of treatment with DMSO, 1 μM BRQ, or 1 μM APH combined with either vehicle, ATRi (20 nM AZ20), ATRi + ATMi (80 nM AZD0156), or Chk1i (100 nM rabusertib). APH, aphidicolin.

I. Percentage of CD11b-expressing ER-Hoxa9 dCas9-KRAB cells following knockdown of p21 (sgCdkn1a) or control guide expression (sgNTC) and treatment with DMSO, 1 μM BRQ, or 1 μM APH for 24 hours.

J. Schematic of experiments testing the effects of compounds in G1-arrested ER-Hoxa9 cells.

K. Median percentage of ER-Hoxa9 cells with at least 5 γH2AX foci after 24h of treatment with DMSO, 1 μM BRQ, 2.5 μM CIS, or 2.5 μg/ml NCS during asynchronous cycling or following G1 arrest in 2 ng/ml SCF. CIS, cisplatin. NCS, neocarzinostatin.

L. Percentage of CD11b-expressing ER-Hoxa9 cells after 24h of treatment with DMSO, 1 μM BRQ, 2.5 μM CIS, or 2.5 μg/ml NCS during asynchronous cycling or following G1 arrest in 2 ng/ml SCF.

Figure 5. Replication stress advances cell fate at the transcriptional level despite limited changes in chromatin accessibility.

A. Principal components analysis (PCA) plot of bulk RNA-sequencing in ER-Hoxa9 cells following 2 μM BRQ treatment or E2 withdrawal for different timepoints.

B. Heat maps showing expression of selected genes in ER-Hoxa9 cells within progenitor modules (GMP and other lineages), maturation modules (myeloid TFs, primary/secondary/tertiary granules), and cell cycle following BRQ treatment or E2 withdrawal for different timepoints.

C. (Top) Smoothed log2 expression of selected GMP and maturation genes along a pseudotime trajectory of normal mouse GMP to neutrophil differentiation, calculated using scRNAseq data from (Xie et al., 2020). (Bottom) Projection of each timepoint from BRQ and -E2 RNA-seq in ER-Hoxa9 cells to the pseudotime trajectory. The point along the GMP-to-neutrophil trajectory to which each timepoint during BRQ and -E2 treatment is most highly correlated is plotted.

D. Heatmap of gene expression in THP-1 cells treated with 500 nM BRQ, 100 µM HU, or 100 nM PMA for the indicated timepoints. Expression of selected granulocyte, macrophage, and progenitor genes is displayed.

E. Heatmap of gene expression in K562 dCas9-KRAB cells transduced with a non-targeting guide (sgNTC) or a guide targeting the *BCR* promoter (sgBCR), or treated with DMSO or 250 nM BRQ for 72h. Expression of selected erythroid genes, mitochondrial import or mitoribosome genes, myeloid genes, or transcription factors is shown.

F. Number of differentially accessible peaks (increased accessibility plotted as positive values and decreased accessibility plotted as negative values) at various timepoints following 2 µM BRQ treatment or E2 withdrawal in ER-Hoxa9 cells. Shared differentially accessible peaks are also plotted.

G. Selected transcription factor motifs and their accessibility scores from ChromVAR analysis of ATAC-seq (same conditions as in F).

H. Same as (F), but for BRQ and PMA treatment in THP-1 cells.

I. Same as (G), but for BRQ and PMA treatment in THP-1 cells.

J. IGV browser screenshots for two representative genes (*Slpi* and *Csf2rb*) in ER-Hoxa9 cells where chromatin accessibility and transcriptional changes are discordant following BRQ treatment. ATAC-seq and RNA-seq signal at baseline and 48h after BRQ treatment or E2 withdrawal are displayed, as well as baseline H3K4me1, H3K27ac, and IgG CUT&RUN signal.

K. (top left) Distribution of expression changes for shared upregulated genes after 48h of BRQ treatment or E2 withdrawal in ER-Hoxa9 cells. (top right) Distribution of the proportion of peaks that gain accessibility for all shared upregulated genes after 48h of BRQ treatment or E2 withdrawal. (bottom left) Scatterplot of expression changes, with several genes highlighted. (bottom right) Scatterplot of the proportion of peaks that gain accessibility. P-values calculated using the Mann-Whitney U test.

Figure 6. Loss of lineage-specific transcription factors redirects the response to replication stress.

A. Percentage of CD11b-expressing ER-Hoxa9 dCas9-KRAB cells expressing sgNTC, sgSpi1-1, or sgSpi1-2 (n=3) after 48h of treatment with DMSO, 1 µM BRQ, 50 µM HU, or 1 µM APH. (****) p <

0.00005, and adjusted p-values were calculated using a two-way ANOVA with the Šidák correction for multiple comparisons.

B. Venn diagram of upregulated genes (|LFC| > 1 and adjusted p-value < 0.01) after 48h of 1μM BRQ treatment of sgNTC or sgSpi1-1 ER-Hoxa9 cells, compared to DMSO.

C. Heatmap showing log fold changes for selected genes in sgNTC, sgSpi1-1, or sgSpi1-2 ER-Hoxa9 cells treated with DMSO or 1 μM BRQ for 48h, relative to the sgNTC DMSO condition (n=4).

D. Percentage of CD235a-expressing K562 dCas9-KRAB cells expressing sgNTC, sgGATA1-1, and sgGATA1-2 (n=3) after 72h of treatment with DMSO, 250 nM BRQ, or 125 μM HU. (****) p < 0.00005, and adjusted p-values were calculated using a two-way ANOVA with the Šidák correction for multiple comparisons.

E. Venn diagram of upregulated genes (|LFC| > 1 and adjusted p-value < 0.01) after 72h of 250 nM BRQ treatment of sgNTC or sgGATA1-1 K562 dCas9 cells, compared to DMSO.

F. Heatmap showing log fold changes for selected genes in sgNTC or sgGATA1-1 K562 cells treated with DMSO or 250 nM BRQ for 72h, relative to the sgNTC DMSO condition (n=3).

Figure 1. A focused pharmacologic screen reveals molecules targeting nucleotide metabolism can promote leukemia differentiation.
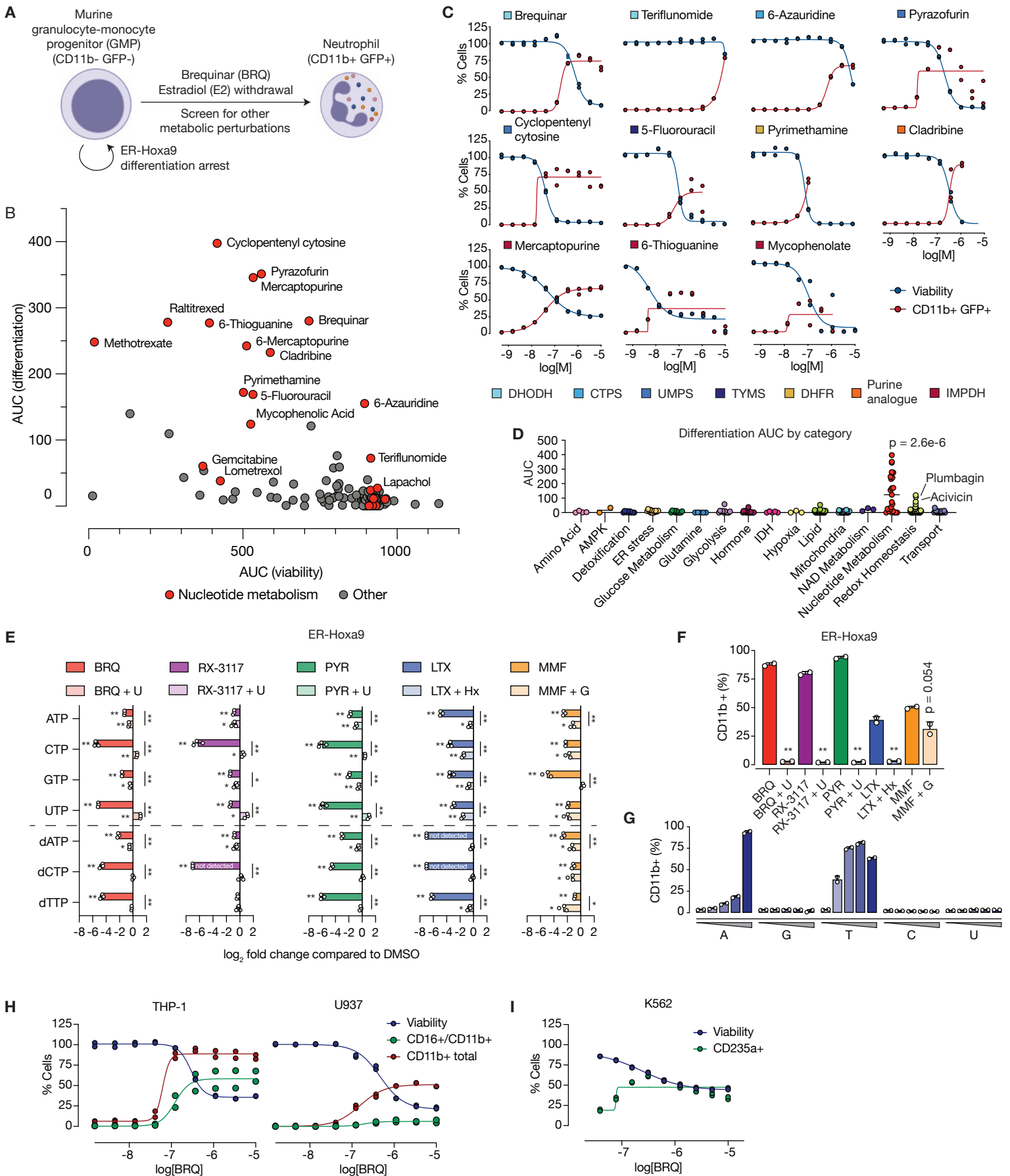
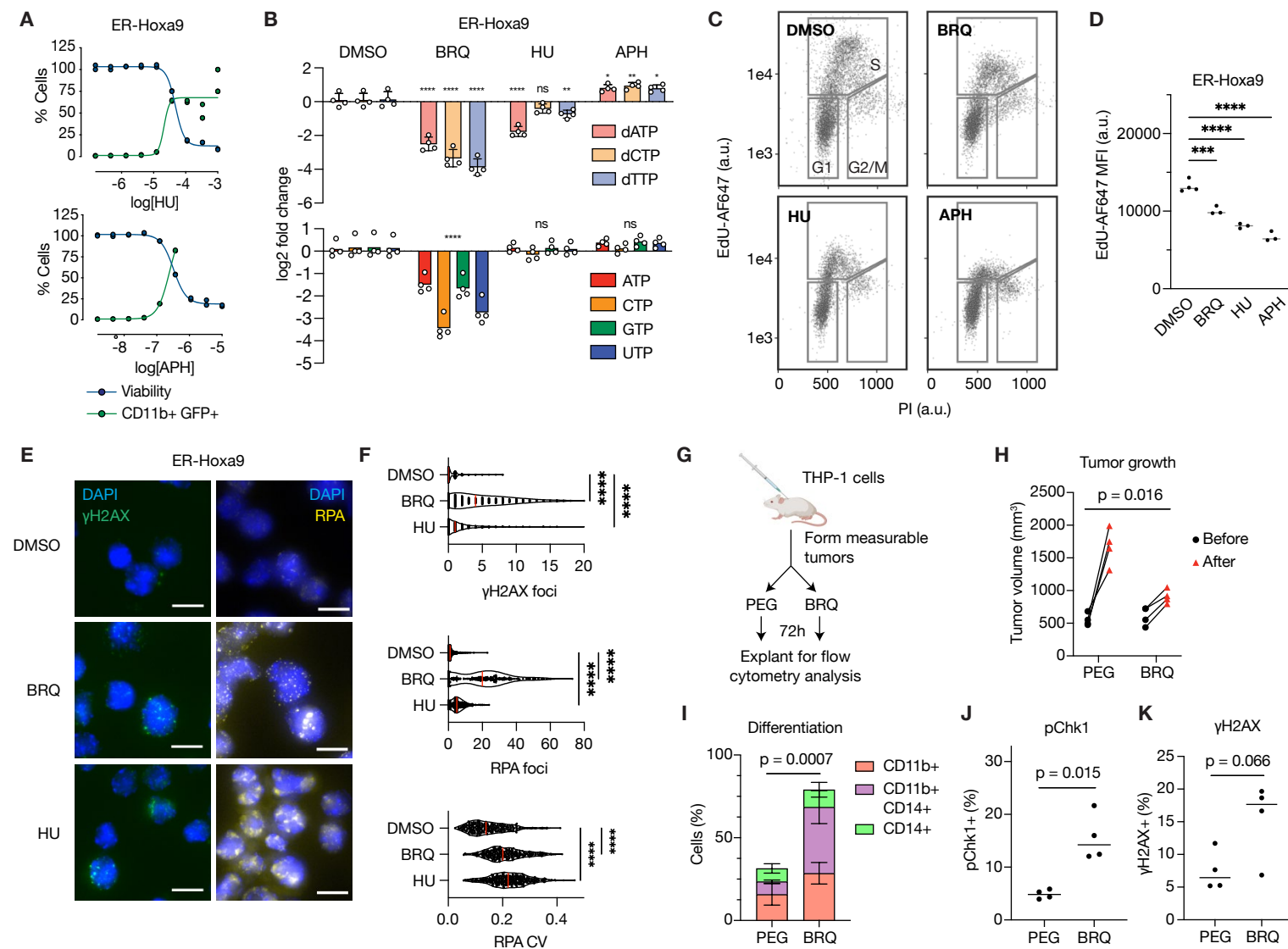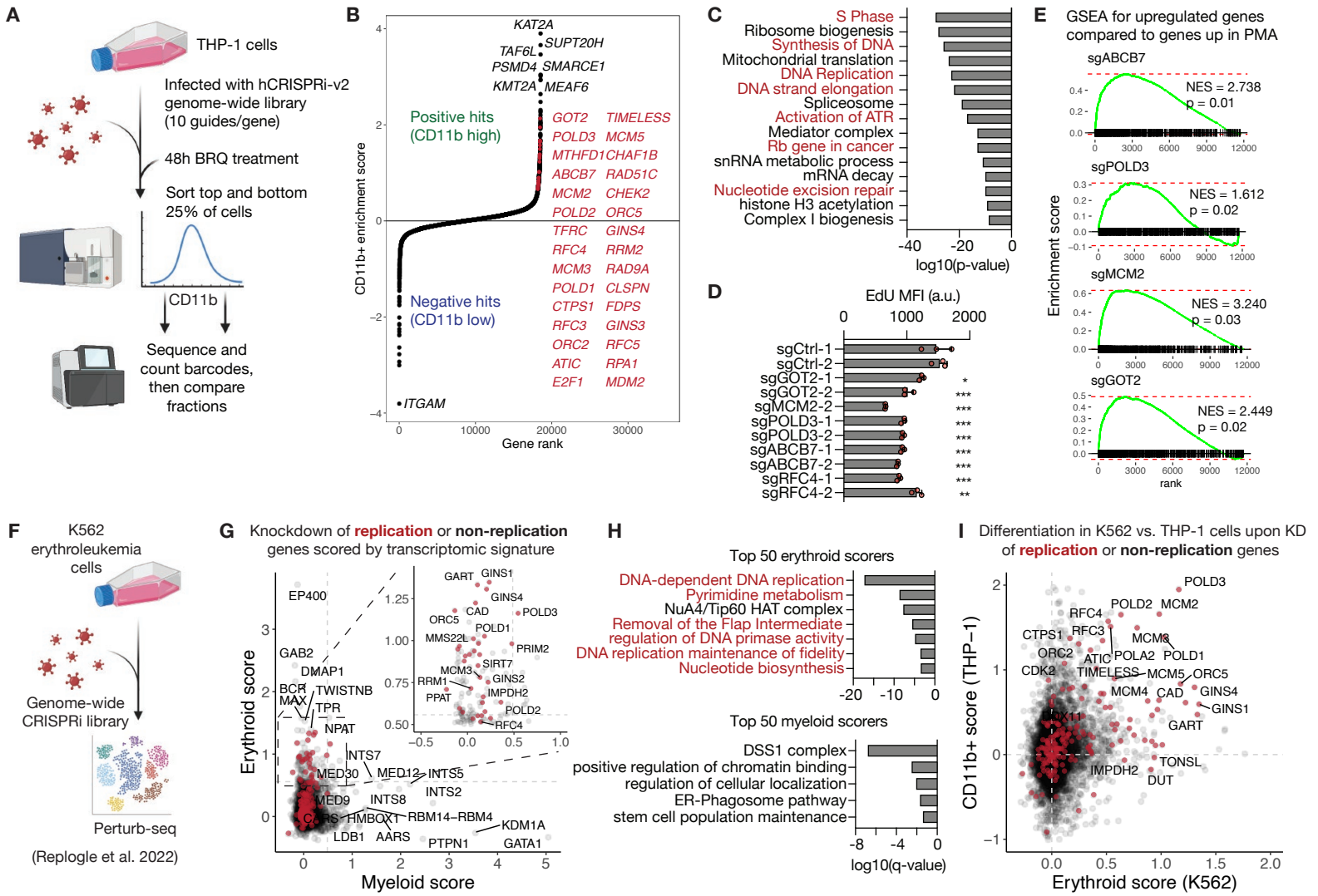**Figure 2.** Replication stress links nucleotide depletion to differential...

Figure 3. Genetic screens demonstrate that depletion of proteins in DNA replication can drive differentiation.

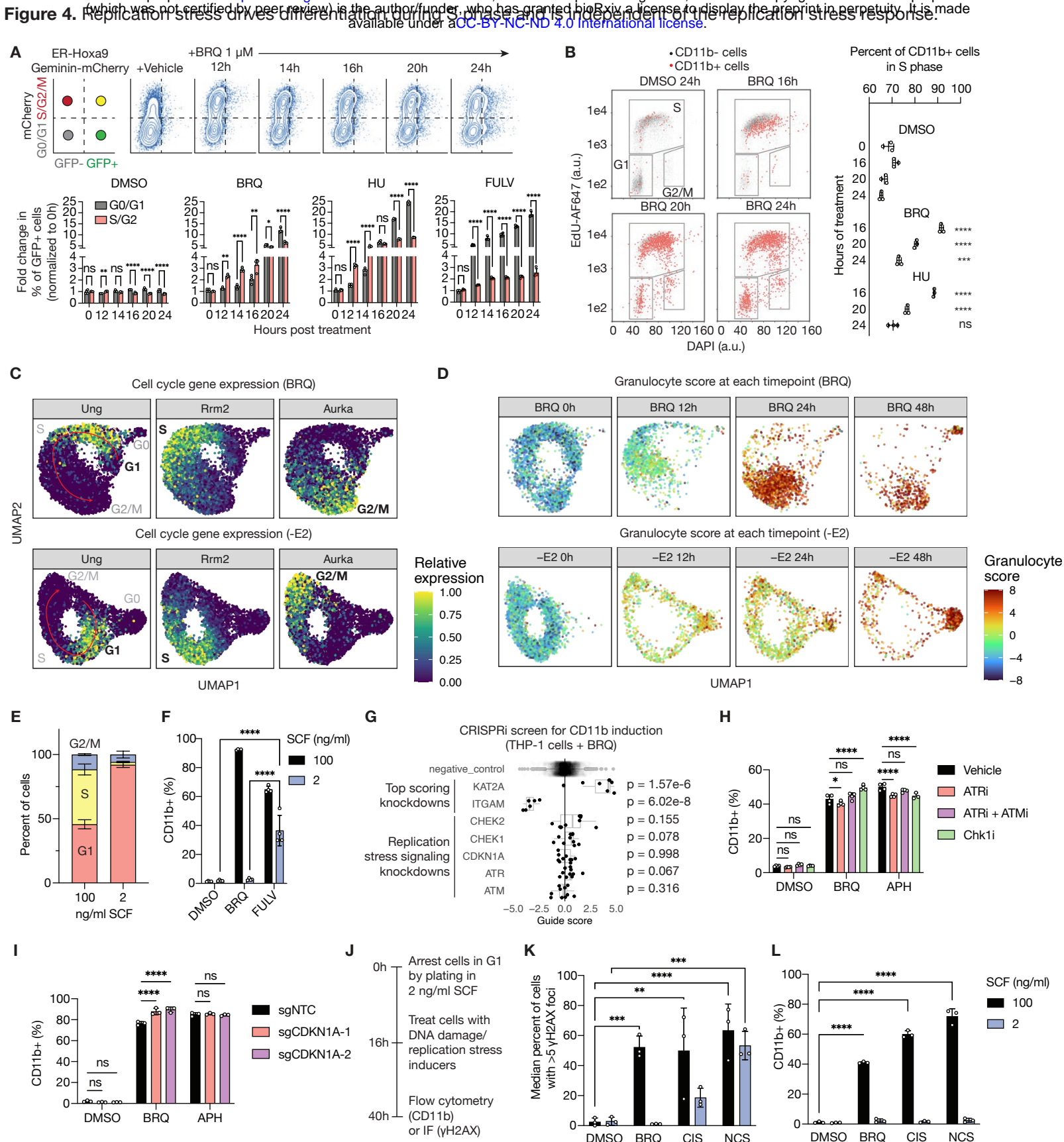**Figure 4.** Replication stress drives differentiation during S phase and is independent on the replication stress response.

Figure 5: Replication stress advances cell fate at the transcriptional and epigenetic level despite limited changes in chromatin accessibility.
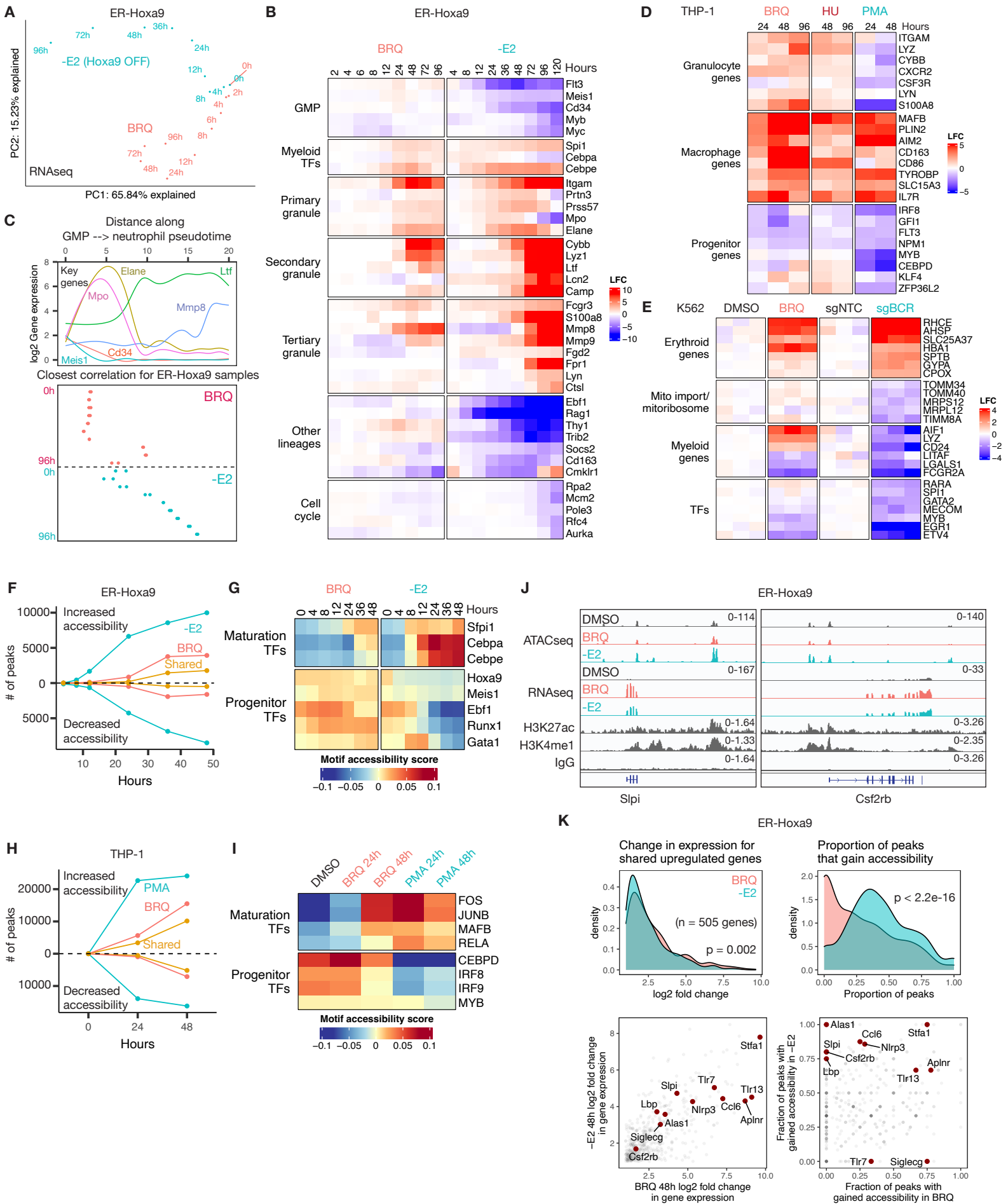
Figure 6. Loss of lineage-specific transcription factors reciprocally response to replication stress.